

# CHARLES UNIVERSITY IN PRAGUE

Faculty of Science

Department of Inorganic chemistry

---



**Jiří Dolanský**

**Nanofiber materials simultaneously photogenerating NO and  $^1\text{O}_2$   
species; Reversible NO binding on boron-containing clusters**

Diploma thesis

Supervisor: Assoc. Prof. Jiří Mosinger, Ph.D.

Consultant: Dr. Michael G. S. Londesborough, B.Sc., Ph.D.

Prague 2014

This master thesis was supported by grant of Academy of Sciences:

GACR P207/11/1577

Grant no. 13-124965

## ***Prohlášení***

Prohlašuji, že jsem předloženou diplomovou prací "**Nanovláknenné materiály simultánně fotogenerující NO a  $^1\text{O}_2$ ; Reverzibilní vázání NO borovými klastry**" vypracoval samostatně a že jsem uvedl veškeré zdroje, ze kterých jsem čerpal. Tato práce ani její podstatná část nebyla předložena k získání jiného nebo stejného akademického titulu. Jsem si vědom toho, že využití výsledků této práce mimo Univerzitu Karlovu v Praze je možné pouze s písemným souhlasem této univerzity.

V Praze, 20.květen 2014

Jiří Dolanský

## *Acknowledgments*

I would like to thank my supervisors Assoc. Prof. Jiří Mosinger, Ph.D. and Dr. Michael G. S. Londesborough, B.Sc., Ph.D. for the opportunity to work and study in their research groups and also for their patience and advice regarding the work in this thesis. I would also like to thank to all my colleagues from both, the Group of Photochemistry and Supramolecular Chemistry of Porphyrinoids (Charles University in Prague) and the Department of Syntheses (Institute of Inorganic Chemistry AS CR. v. v. i.) for creating a pleasant working atmosphere. Next thanks goes to RNDr. Ivana Císařová, Ph.D. and RNDr. Marek Nečas, Ph.D. for single-crystal X-ray diffraction measurements, RNDr. Pavel Kubát, CSc. for time-resolved phosphorescence of  $^1\text{O}_2$  measurements, prof. Salvatore Sortino for amperometric NO measurements, Dr. Petr Henke for antibacterial tests, Dr. Jens Langecker, Ph.D. for  $^{31}\text{P}$  NMR measurements and his help and advices during syntheses. Last but not least thanks go to my family, friends and girlfriend for being supportive during my studies.

## ***Abstrakt***

V této práci byly připraveny a charakterizovány polystyrenové nanovláknenné materiály s kovalentně vázaným NO-fotodonorem a elektrostaticky vázaným tetrakationtovým porfyrinoidním fotosensitizerem. Tyto fotofunkční materiály mají schopnost simultánně fotogenerovat antibakteriální molekuly NO a  $O_2(^1\Delta_g)$  na denním světle, a tím sterilizovat svůj povrch a blízké okolí. Nanovláknenné materiály byly studovány pomocí SEM, FTIR, emisní a UV/vis spektroskopie a pomocí časově rozlišené emisní a absorpční spektroskopie. Antibakteriální efekt byl testován na *Escherichia coli*. Kombinace duální antibakteriální schopnosti a nanoporézní charakter nanovláknenného materiálu, zadržující patogeny jako např. bakterie na svém povrchu, umožňuje tyto materiály využít v oblastech, kde je vyžadováno sterilní prostředí (roušky, kryty ran atd.).

Pro studium vázání NO byl připraven v literatuře již popsáný bimetallický boranový klastr  $(PMe_2Ph)_4Pt_2B_{10}H_{10}$ , který má schopnost reverzibilně vázat malé plynné molekuly. Úspěšně bylo syntetizováno sedm nových monometallických prekurzorů (s Pt, Pd či Ni) pro syntézu bimetallických boranových klastrů s účelem studia reverzibilního vázání NO. Všechny látky byly chromatograficky přečištěny a charakterizovány pomocí NMR spektroskopie a rentgenové difrakční analýzy.

**Klíčová slova:** singletový kyslík, oxid dusnatý, nanovláknna, fotosensitizer, metalla-borany

## ***Abstract***

This project is concerned with the preparation of electrospun polystyrene (PS) nanofiber materials with covalently bonded NO-photodonor and electrostatically attached tetracationic porphyrinoid photosensitizers. These photofunctional nanofiber materials exhibit effective simultaneous photogeneration of small antibacterial NO and  $O_2(^1\Delta_g)$  species under irradiation with daylight creating an antibacterial surface and near surrounding. NO species can be also generated just by gentle heating. Nanofiber materials were analyzed with SEM, FTIR, emission and UV/vis spectroscopy and time-resolved emission and absorption spectroscopy. The antibacterial effect was tested on *Escherichia coli*. The dual antibacterial action, in combination with the nanoporous character of the material that detains pathogens like bacteria on its surface, is ideal for any application where a sterile environment is necessary.

The known bimetallic cluster system  $[(PMe_2Ph)_4Pt_2B_{10}H_{10}]$  that possesses the propensity to reversibly bind small gaseous molecules ( $O_2$ ,  $SO_2$ , CO) was synthesized in good yields for NO reversible binding investigation. Seven new monometallic precursors (Pt, Pd and Ni) to new bimetallic species were successfully synthesized with the aim of future study of NO reversible binding. All new compounds were purified by chromatographic methods and characterized by multinuclear NMR spectroscopy and single-crystal X-ray diffraction analysis.

**Keywords:** singlet oxygen, nitric oxide, nanofibers, photosensitizer, metallaboranes

# ***Content***

<b>List of abbreviations</b>	<b>7</b>
<b>1. Introduction</b>	<b>8</b>
1. 1. Singlet oxygen	8
1. 2. Photosensitized generation of singlet oxygen	9
1. 3. O <sub>2</sub> ( <sup>1</sup> Δ <sub>g</sub> ) detection methods	11
1. 4. Photoactive nanofiber materials producing O <sub>2</sub> ( <sup>1</sup> Δ <sub>g</sub> )	11
1. 5. Nitric oxide	12
1. 6. Donors of NO	13
1. 7. Photodonors of NO	13
1. 8. Systems for NO reversible binding	15
1. 8. 1. <i>nido</i> -7-metallaundecaboranes as dimetallaborane precursors	16
1. 8. 2. <i>closo</i> -1,2-dimetalladodecaboranes	18
1. 9. NO detection methods	21
1. 10. Materials simultaneously photoreleasing O <sub>2</sub> ( <sup>1</sup> Δ <sub>g</sub> ) and NO	22
<b>2. The aims of the study</b>	<b>25</b>
<b>3. Experimental section</b>	<b>26</b>
3. 1. Chemicals and materials	26
3. 2. Synthetic procedures	26
3. 3. Electrospinning	29
3. 4. Scanning Electron Microscopy (SEM)	29
3. 5. Ion exchange capacity (IEC) with adsorption kinetics	29
3. 6. Fourier transform infrared spectra (FTIR)	29
3. 7. UV/vis absorption and fluorescence spectroscopy	29
3. 8. Photooxidation of model species by nanofiber materials	30
3. 9. Chemical detection of NO	30
3. 10. The time-resolved near-infrared phosphorescence of O <sub>2</sub> ( <sup>1</sup> Δ <sub>g</sub> )	30
3. 11. Amperometric detection of NO	31

3. 12. Antibacterial tests	31
3. 13. NMR Spectroscopy	31
3. 14. Chromatography	32
3. 15. Single-crystal X-ray Diffractometry	32
3. 16. Software	32
<b>4. Results and discussion for Aim I</b>	<b>33</b>
4. 1. Preparation, IEC and morphology of nanofiber materials	33
4. 2. ATR-FTIR spectra	36
4. 3. UV/vis spectra	37
4. 4. O <sub>2</sub> ( <sup>1</sup> Δ <sub>g</sub> ) detection	38
4. 5. NO detection	40
4. 6. Antibacterial activity	42
<b>5. Results and discussion for Aim II</b>	<b>44</b>
5. 1. Reversible binding of NO onto dimetallaborane [ <i>clos</i> o-(PMe <sub>2</sub> Ph) <sub>4</sub> Pt <sub>2</sub> B <sub>10</sub> H <sub>10</sub> ]	44
5. 2. Preparation of new monometallaborane species	47
5. 2. 1. NMR data	49
5. 2. 2. General considerations on bond connectivity lengths and bond angles	54
5. 2. 3. The choice of ligand in the syntheses of new 11-vertex metallaborane compounds	55
<b>6. Conclusions</b>	<b>57</b>
<b>7. References</b>	<b>58</b>

## ***List of abbreviations***

<b>bdmn</b>	N,N,N',N'-tetramethyl-1,8-naphthalenediamine	<b>TLC</b>	thin-layer chromatography
<b>CFU</b>	colonies formation units	<b>TMPyP</b>	(5,10,15,20-tetrakis( <i>N</i> -methylpyridinium-4-yl)porphyrin tetra( <i>p</i> -toluenesulfonate)
<b>DAN</b>	2,3-diaminonaphthalene	<b>UV/vis</b>	ultraviolet–visible spectroscopy
<b>FTIR</b>	fourier transform infrared spectroscopy	<b>ZnPcI<sub>4</sub></b>	Zinc(II) 2,9,16,23-tetrakis( <i>N</i> -methylpyridiumoxy)phthalocyanine tetraiodide
<b>IEC</b>	ion exchange capacity		
<b>Mb</b>	myoglobine		
<b>MeLi</b>	methyllithium		
<b>MS</b>	mass spectroscopy		
<b>NAT</b>	2,3-naphthotriazole		
<b>NMR</b>	nuclear magnetic resonance		
<b>NOP</b>	N-(3-aminopropyl)-3-(trifluoromethyl)-4-nitrobenzenamine		
<b>O<sub>2</sub>(<sup>1</sup>Δ<sub>g</sub>)</b>	singlet oxygen with longer lifetime		
<b>O<sub>2</sub>(<sup>1</sup>Σ<sub>g</sub><sup>+</sup>)</b>	singlet oxygen with shorter lifetime		
<b>PDT</b>	photodynamic therapy		
<b>PLGH</b>	poly(lactic-co-glycolic-co-hydroxymethyl propionic acid		
<b>PS</b>	polystyrene		
<b>SEM</b>	scanning electron microscope		



# 1. Introduction

## 1. 1. Singlet oxygen

Singlet oxygen is a short-lived and highly oxidative cytotoxic species that has received remarkable attention from chemists and biochemists for its interesting mechanistic and synthetic aspects and large environmental, biological and medical significance. Its high reactivity is caused by the fact that the reactions between singlet oxygen and the majority of chemical compounds are spin-allowed. On the contrary, reactions of common triplet dioxygen  $O_2(^3\Sigma_g^-)$  with most of the compounds are spin-forbidden.<sup>1</sup>

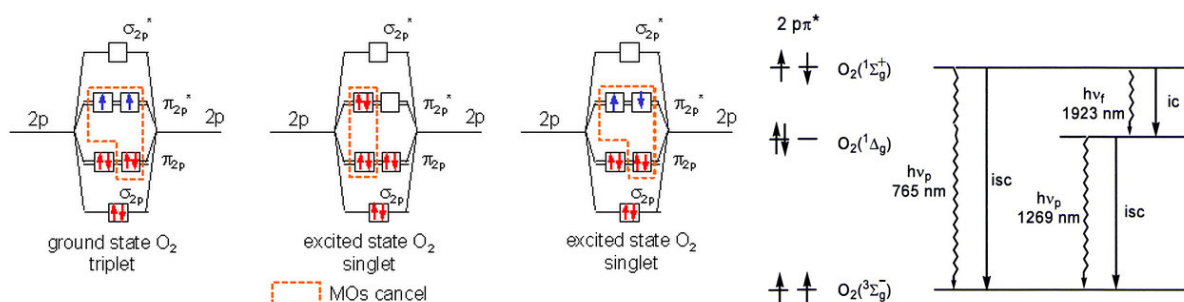


**Figure 1. 1.** Diagrams of dioxygen molecule orbitals (A) and the Jablonski scheme (B) with corresponding radiative (direct arrows) and nonradiative (wave arrows) transitions (*ic* internal conversion, *isc* intersystem crossing).

**Figure 1. 1.**, depicts the two existing forms of singlet oxygen:  $O_2(^1\Delta_g)$ , which has a longer lifetime and state energy of  $94.1 \text{ kJ} \cdot \text{mol}^{-1}$ , and the less stable  $O_2(^1\Sigma_g^+)$ , which has a short lifetime and higher associated energy of  $156.9 \text{ kJ} \cdot \text{mol}^{-1}$ .<sup>2</sup>

The transition from the  $O_2(^1\Delta_g)$  state to the  $O_2(^1\Sigma_g^-)$  state is spin forbidden, therefore the  $O_2(^1\Delta_g)$  is a relatively long-lived species. The second excited state of oxygen, on the other hand, is short-lived due to a spin-allowed transition to the  $O_2(^1\Delta_g)$  state. This difference in stability is confirmed by the radiative lifetimes of  $O_2(^1\Delta_g)$  and  $O_2(^1\Sigma_g^+)$ ; which are  $\approx 64 \text{ min}$  and  $10 - 12 \text{ s}$  in the gas phase, respectively. It follows that it is mostly  $O_2(^1\Delta_g)$  that participates in photooxidation reactions.<sup>1,3</sup>

Studies have shown that the lifetimes of both states of singlet oxygen are highly dependent on the nature of the environment. Generally, surroundings/solvents with OH groups quench  $O_2(^1\Delta_g)$  more effectively ( $\tau_\Delta$  in a range of  $\mu\text{s}$ ), however in weakly interacting halogenated hydrocarbons,  $O_2(^1\Delta_g)$  can persist for tens of milliseconds. The lifetime of  $O_2(^1\Delta_g)$  in air is in the range of  $\mu\text{s}$  (**Table 1. 1.**).<sup>4,5</sup>

**Table 1. 1.** - Properties of two lowest electronic states of singlet oxygen<sup>3</sup>

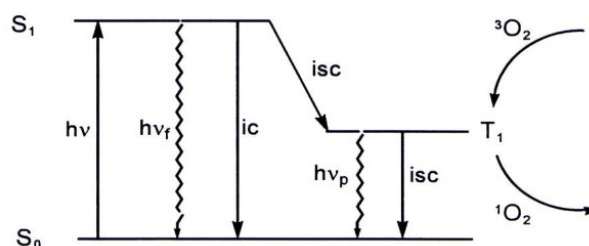
	$O_2(^1\Delta_g)$	$O_2(^1\Sigma_g^+)$	
<b>Energy (kJ mol<sup>-1</sup>)</b>	94.1	156.9	
<b>Transition in solution (nm)</b>	$O_2(^1\Delta_g) \rightarrow O_2(^3\Sigma_g^-)$ 1269 - 1282	$O_2(^3\Sigma_g^+) \rightarrow O_2(^3\Sigma_g^-)$ 765	$O_2(^3\Sigma_g^+) \rightarrow O_2(^1\Delta_g)$ 1914-1936
<b><math>\tau_r</math> (gas)<sup>a</sup></b>	64 - 65 min	10 - 12 s	6.7 min
<b><math>\tau_r</math> (solution)<sup>a</sup></b>	0.25 - 10 s	1 s	0.33 - 1.4 ms
<b><math>\tau_A</math> (H<sub>2</sub>O)<sup>b</sup></b>	3.1 - 4.2 $\mu$ s	8.2 ps	
<b><math>\tau_A</math> (D<sub>2</sub>O)<sup>b</sup></b>	55 - 68 $\mu$ s	42 ps	

<sup>a</sup> Radiative lifetime<sup>b</sup> Natural lifetime

Singlet oxygen can be generated by many ways, *e. g.* by microwave discharge in the oxygen atmosphere<sup>1</sup>, photolysis of ozone<sup>6</sup>, thermolysis of endoperoxides<sup>7</sup>, *via* chemical reactions *e. g.* using H<sub>2</sub>O<sub>2</sub>/ClO<sup>-</sup>, H<sub>2</sub>O<sub>2</sub>/MoO<sub>4</sub><sup>2-</sup> and H<sub>2</sub>O<sub>2</sub>/CaO<sub>2</sub> systems<sup>8</sup>, *etc.* Nevertheless, probably the most convenient method for the generation of O<sub>2</sub>(<sup>1</sup>Δ<sub>g</sub>) is by photosensitized reactions.<sup>3</sup>

## 1. 2. Photosensitized generation of singlet oxygen

Dioxygen characteristically absorbs UV radiation in a vacuum at 147 nm; a wavelength that cannot be directly excited by usual sources of UV/vis radiation. Nevertheless, it can be excited indirectly *via* photosensitized reactions. The mechanism includes the formation of the photosensitizer triplet state and transfer of energy to triplet oxygen leading to O<sub>2</sub>(<sup>1</sup>Δ<sub>g</sub>) formation.<sup>8</sup> The simplified photosensitized generation of singlet oxygen is shown in **Figure 1. 2.**<sup>2</sup>

**Figure 1. 2.** Photosensitized singlet oxygen production (ic internal conversion, isc intersystem crossing).<sup>8</sup>

Photosensitizer excitation is generally achieved *via* a one-photon adsorption ( $h\nu$ ) of the ground state, S<sub>0</sub>, to singlet excited states S<sub>n</sub>. Fast relaxation of the S<sub>n</sub> states yields the lowest excited singlet state of the photosensitizer S<sub>1</sub>. Intersystem crossing (isc) generates the photosensitizer in the triplet state (T<sub>1</sub>). A significantly longer lifetime of the T<sub>1</sub> state, typically in

the range of  $\mu\text{s}$ - $\text{ms}$ , compared to  $S_1$  state ( $\text{ns}$ ) is the basic prerequisite for efficient energy transfer to  $\text{O}_2(^3\Sigma_g^-)$  giving  $\text{O}_2(^1\Delta_g)$ .<sup>1</sup>

Numerous photosensitizers such as eosine, acridine, rose bengal, methylene blue, perylenequinones, triarylmethane dyes *etc.*<sup>9,10</sup> efficiently photogenerate singlet oxygen, nevertheless, the majority of photosensitizers investigated in the context of medical and biological applications were compounds with a porphyrinoid structure.<sup>11,12</sup> The reason for this preference is the extensive knowledge of their chemistry together with the similarity to natural porphyrins frequently occurring in living matter as well as their strong absorption in the VIS region.

Photosensitized reactions of porphyrinoids are applied in many areas such as photodynamic therapy (PDT) of cancer or atherosclerosis,<sup>12,13,14</sup> photodynamic inactivation of pathogenic microorganisms,<sup>15</sup> blood disinfection,<sup>16</sup> and sun-light activated insecticides and pesticides.<sup>17</sup> The photodynamic effect rests in the oxidative damage of a biological target, predominantly by  $\text{O}_2(^1\Delta_g)$  generated *in situ* by photosensitized reactions. Appropriate chemical and photophysical properties of a porphyrinoid photosensitizer such as spectral characteristics, photochemical stability and reasonable quantum yields of singlet oxygen formation ( $\Phi_\Delta$ ) are prerequisites for effective photodynamic action. Some of water-soluble porphyrinoids are photosensitizers with high  $\Phi_\Delta$ <sup>18,19</sup> with potential applications in biology and medicine<sup>20</sup>. The tendency of porphyrinoids to spontaneously aggregate especially in aqueous environment is not desirable since the photodynamic efficiency decreases as a result of the poor or absent ability of dimer and higher aggregates to produce  $\text{O}_2(^1\Delta_g)$ .<sup>21</sup> Binding of porphyrinoid photosensitizers to biopolymers and/or transporting carriers is a subject of recent studies since the binding can cause changes in the physico-chemical and photophysical properties of the photosensitizers and can prevent aggregation.<sup>20,22</sup>

Cationic porphyrinoids have attracted considerable attention as effective photosensitizers.<sup>23</sup> Due to their binding affinity towards nucleic acids, these porphyrins can selectively photocleave DNA<sup>24,25</sup> and inhibit telomerases.<sup>26,27</sup> The photoinactivation of extremely resistant bacteria<sup>28,29</sup> and antiviral activity<sup>30,31</sup> were also reported.

### 1. 3. O<sub>2</sub>(<sup>1</sup>Δ<sub>g</sub>) detection methods

It is generally assumed that time-resolved spectroscopy is one of the most reliable methods of O<sub>2</sub>(<sup>1</sup>Δ<sub>g</sub>) detection and kinetics. O<sub>2</sub>(<sup>1</sup>Δ<sub>g</sub>) exhibits phosphorescence centered at 1270 nm (**Figure 1. 1.**) that can be directly observed and followed. The transition of singlet oxygen to the ground state is strongly spin-forbidden, depending on the surrounding environment. D<sub>2</sub>O is often used as a solvent for O<sub>2</sub>(<sup>1</sup>Δ<sub>g</sub>) phosphorescence detection due to longer O<sub>2</sub>(<sup>1</sup>Δ<sub>g</sub>) lifetime (>60μs) and corresponding stronger signal of phosphorescence in this media.<sup>32</sup>

Many other suitable physical and chemical techniques can be employed.<sup>8</sup> Besides other chemical methods, singlet oxygen formation can be followed using the simple and sensitive iodide method.<sup>33,34</sup> The amount of photoproduced I<sub>3</sub><sup>-</sup> (followed at its bands at 287 and 351 nm) is directly proportional to the concentration of generated O<sub>2</sub>(<sup>1</sup>Δ<sub>g</sub>). Although this method is very sensitive, it is not specific for O<sub>2</sub>(<sup>1</sup>Δ<sub>g</sub>). Specific chemical detection can be achieved using photobleaching of uric acid, a known O<sub>2</sub>(<sup>1</sup>Δ<sub>g</sub>) acceptor.<sup>4</sup> The decrease of the absorption band associated with uric acid at 292 nm is proportional to the amount of generated O<sub>2</sub>(<sup>1</sup>Δ<sub>g</sub>).

### 1. 4. Photoactive nanofiber materials producing O<sub>2</sub>(<sup>1</sup>Δ<sub>g</sub>)

During the last decade, electrospinning has attracted great interest among academic and industrial scientists because it is a very simple, low cost, and effective technology to produce polymer nanofibers. Due to their exceptional properties such as large surface area, low weight, and low cost, these materials have found a wide range of uses: in the fields of protective clothing<sup>35</sup>, drug carriers<sup>36</sup>, medicine<sup>37</sup>, and sensing<sup>38</sup> for example.

Recently, in our laboratory we have developed nanofiber materials with encapsulated or ionically attached porphyrinoid photosensitizers that generate O<sub>2</sub>(<sup>1</sup>Δ<sub>g</sub>) in high quantum yield upon irradiation by visible light. Photogenerated short-living, highly cytotoxic O<sub>2</sub>(<sup>1</sup>Δ<sub>g</sub>) efficiently kill bacteria such as *Escherichia coli*, *Staphylococcus aureus*, *Pseudomonas aeruginosa*<sup>29,39,40,41,42</sup> non-enveloped polyomaviruses and enveloped baculoviruses<sup>43</sup> on the surface of such nanofiber materials. Electrospun materials with a nanofiber diameter *ca.* 100-400 nm have a high surface area, good transparency to light; usually higher oxygen permeability/diffusion and nanoporous structure,<sup>44</sup> which prevents the passing of bacteria and other pathogens through the nanofiber materials as they are detained on the surface.<sup>29</sup> The small diameter of the nanofibers allows the efficient diffusion of O<sub>2</sub>(<sup>1</sup>Δ<sub>g</sub>) through the nanofibrous polymer, enabling higher oxygen permeability/diffusion followed by photooxidation of chem-

ical or biological targets<sup>45,46</sup> Currently, these nanofiber materials were successfully applied to dermatology as antibacterial wound covering activated by light.<sup>42</sup>

One of the most efficient antibacterial effect exhibited sulfonated polystyrene nanofiber material with externally bounded cationic 5,10,15,20-tetrakis(*N*-methylpyridinium-4-yl)porphyrin tetra(*p*-toluenesulfonate) (TMPyP) photosensitizer (**Figure 1. 3.**)<sup>29</sup> These materials are similar to the ones studied in this project.

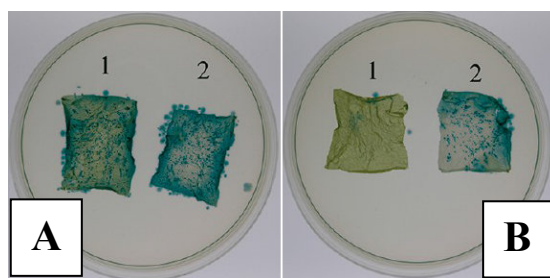


**Figure 1. 3.** Antibacterial activity of the surface of sulfonated polystyrene nanofiber material with ionically attached TMPyP (1) or sulfonated material without TMPyP (2) when (B) irradiated with a 400 W solar simulator for 2 minutes or (A) stored in the dark. The samples were inoculated with the *E. coli* strain DH5 $\alpha$  (blue-green spots) before irradiation.<sup>29</sup>

Although a wide spectrum of polymers can be used for preparation of nanofibers, only a few are suitable as inert matrices for photoactive compounds. One of the most appropriate polymer is the low cost, chemically well defined, polystyrene (PS) which has excellent optical transparency and can be functionalized by post-processing modifications: chlorosulfonation or sulfonation.<sup>47</sup> Moreover, both sulfonated and especially chlorosulfonated PS can be further modified. Chlorosulfonation in particular opens more ways for the further functionalization, which has been studied on transparent PS thin layers (**Figure 1. 4.**)<sup>47</sup> but not on nanofiber materials.

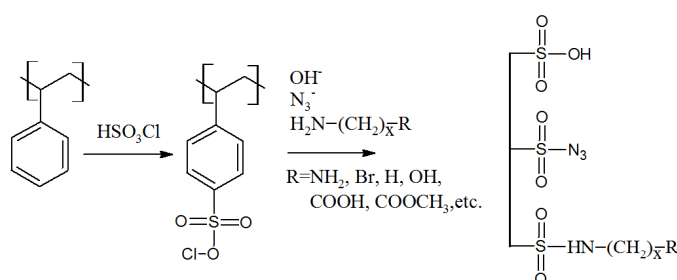


**Figure 1. 4.** Possible approaches for preparation of functionalized PS substrates.

### 1. 5. Nitric oxide

NO has many interesting properties and functions (**Figure 1. 5.**) which can be applied in medicine. Its main features include its anti-microbial and vasodilatation properties<sup>48</sup>, its charge neutrality, small molecular size, its lifetime of around 4s in air, and its diffusion radius

of about 100  $\mu\text{m}$ .<sup>48</sup> Over the past 15 years the influence of NO on the outcome of cancer therapies dependent on oxygen and the generation of reactive oxygen species, such as PDT, has been studied.<sup>49</sup> Elevated NO levels may maintain vessel dilation during PDT treatment, resulting in increased tumour oxygenation, thereby enhance phototoxic damage.<sup>50</sup>

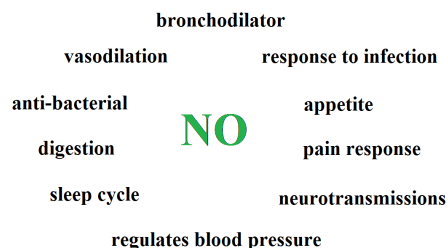


**Figure 1. 5.** Nitric oxide and its functions.

### 1. 6. Donors of NO

While generation of  $\text{O}_2(^1\Delta_g)$  is based on photophysical processes, in principle, without chemical changes in the photosensitizer, generation of NO implies a chemical reaction with resulting degradation of the donor centre.

In general, nitric oxide donors are compounds that store NO in an air-stable form. Over 15 types of NO donor classes exist *e. g.* nitrosothiols, oximes, organic nitrates, *etc.*<sup>51</sup> These NO donors store and release NO through various mechanisms, and an understanding of these basic mechanisms is important when choosing the ideal NO donor for any application. For example, organic nitrates release NO by a three-electron reduction, which can be performed *via* either an enzymatic or non-enzymatic pathway. Organic nitrites generate NO by a one-electron reduction by hydrolyzing nitrite that then is reduced to NO. Metal-NO compounds release NO by enzymatic reduction or one electron reduction by thiols or hemoproteins. Oximes release NO through a proposed radical decomposition at basic pH.<sup>52</sup>

Through experimental studies, NO donor molecules were used to demonstrate the validity that NO has a strong anti-microbial activity *in vivo*. NO releasing compounds were shown to successfully inhibit or kill microbes and the anti-microbial activity of NO was demonstrated to be effective against viruses, bacteria, fungi and parasites.<sup>53</sup>

### 1. 7. Photodonors of NO

For the purposes of antibacterial materials, the fundamental criteria for NO-releasing molecules are rapid and precise spatiotemporal control of NO delivery. These criteria are best met by light as the most elegant and noninvasive on/off trigger. Furthermore, photons do not affect important physiological parameters (pH, temperature and ionic strength), which is a critical condition for bio-applications.

Metal-NO-donors (Ru, Fe, Mn) can release NO under irradiation with light. Iron and manganese NO-photodons are photosensitive and less stable and need to be protected and stored in the dark.<sup>54</sup> S-nitrosothiols can decompose by thermal, photochemical and copper-mediated decomposition. In the class of the amphiphilic nitrobenzen photodons, the twisted geometry of the NO<sub>2</sub> group with respect to the aromatic plane, due to the presence of the CF<sub>3</sub> substituent, is the key to NO photorelease (**Figure 1. 6.**). Nitro to nitrite photorearrangement is followed by the rupture of the O–NO bond leading to the generation of NO and a phenoxyl radical.<sup>55</sup>

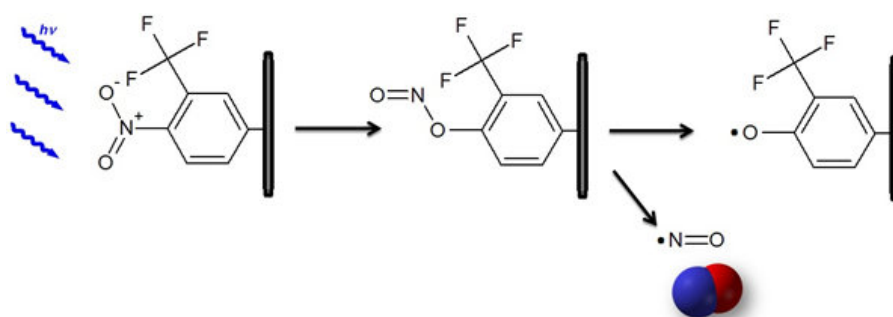


**Figure 1. 6.** Idealized view for the NO photoreleasing on the amphiphilic nitrobenzen photodonor.

Many studies were published in the last decade about NO photoreleasing systems *e. g.* with NO-photodons immobilized as a monolayer on solid supports such a noble metals *via* thiol groups<sup>56</sup>, multilayers of cationic amphiphilic NO-photodons on quartz substrates<sup>57</sup>, fluorophore/photochrome dyads encapsulated within the hydrophobic interior of polymer nanoparticles<sup>58</sup> or supramolecular hydrogel loaded with NO-photodonor<sup>59</sup>. One interesting approach is to use {RuNO}<sup>6</sup> nitrosyl complexes that can be used to functionalize the surface of a multiwalled carbon nanotube and release NO under daylight.<sup>60</sup> All listed materials exhibit strong antibacterial activity with the potential for medicinal uses.

However, there are only several studies regarding polymer materials modified with NO-photodons. High surface area and a nanoporous structure are big advantages that provide a high concentration of photoactive compounds and prevent bacteria and other pathogens passing through the nanofiber materials as they are detained on the surface and killed by photogenerated NO. Polymeric nanofiber materials with covalently attached S-nitrosothiols were prepared *via* thiolation or S-nitrosation of the biodegradable polymer poly(lactic-co-glycolic-co-hydroxymethyl propionic acid (PLGH) and subsequently electrospun. The resulting materials exhibit a stronger bactericidal effect<sup>61</sup> than using NO-releasing xerogels.<sup>62</sup> This can serve as a one evidence of higher potential in using polymeric nanofiber materials than other above mentioned systems.

Transition metal complexes (*e. g.* ruthenium nitrosyls) possess high photostability but poor water solubility which limits their application as NO-photodons in a biological environment. The encapsulation into a biodegradable polymer matrix (*e. g.* poly(L-lactide-co-D/L-lactide) made photorelease of NO to an aqueous solution possible, and the antibacterial activity was subsequently confirmed. Irradiation with UV light results in the release of NO and a Ru(III) photoproduct.<sup>54,63</sup>

Various ruthenium nitrosyls were encapsulated into methacrylate-based polymers. The resulting material is stable, resistant to biological buffer components and exhibit good NO donor ability under UV light. However, nitrosyls slowly diffuse out of the methacrylate medium and contaminate its surroundings within hours.<sup>63</sup> Hence, covalent bonding might be a better approach. Moreover, using visible light as a trigger of NO release is desirable since UV light itself can be employed to kill bacteria and other pathogens.

Nanofibrous gelatin matrix functionalized with S-nitrosothiol is another example of photoactive nanofiber material releasing NO. Gelatin is a nonimmunogenic biopolymer derived from collagen with a unique gelation property due to its triple helix conformation and high water absorption capacity and is able to promote wound healing. One drawback lies in necessity of removal the trace amounts of metal ions ( $\text{Ca}^{2+}$ ,  $\text{Cu}^{2+}$ ,  $\text{Fe}^{2+}$ ) for higher porosity and the high capacity for NO-photodonor. NO can be photoreleased from this material under visible light (absorption maximum at 527 nm). The effective clearing of *Staphylococcus aureus* was subsequently observed by means of light-triggered NO delivery.<sup>64</sup>

### 1. 8. Systems for NO reversible binding

The reversible binding of small molecules on metal atoms, metal-metal vectors, and metal surfaces is often used, both in Nature and in industry, to overcome otherwise insurmountable thermodynamic barriers in chemistry. Examples of uses found for this type of interaction are numerous and perhaps the most important one is the reversible uptake of dioxygen on the iron center in hemoglobin. And because the releasing of NO from its donors causes irretrievable chemical changes, it might be desired to possess the system that would be able to repeatedly release NO and then be saturated again. One possible system that might meet these requirements is based on boron containing clusters. In the last decade, studies regarding bimetalaboranes derived from *nido*-decaborane reported reversible uptake of various gases by the metal-metal linkage in the intensely dark purple icosahedral twelve-vertex bimetalaborane cluster compound  $[(\text{PMe}_2\text{Ph})_4\text{Pt}_2]\text{B}_{10}\text{H}_{10}$ .<sup>65</sup>



Because of its high stability, ready synthesis, and chemical versatility *nido*-decaborane ( $B_{10}H_{14}$ , **Figure 1. 7.**) is the most examined polyhedral borane. It is a volatile, colourless, crystalline compound with a strong characteristic odour, insoluble in water but soluble in many organic solvents. Structurally, its geometry may be formally derived by the removal of two adjacent {BH} vertices from the icosahedral  $[B_{12}H_{12}]^{2-}$ , and replacement of these vertices by four bridging hydrogen atoms over the „open face“ of the cluster. These bridging hydrogen atoms have acidic character. In basic solutions decaborane has properties of a monobasic acid ( $pK_a = 2.7$  - similar to  $ClCH_2COOH$ ).<sup>66</sup> Decaborane is commonly synthesized *via* pyrolysis of lower boron hydrides ( $B_2H_6$  or  $B_5H_9$ ) with a loss of dihydrogen.<sup>67</sup>

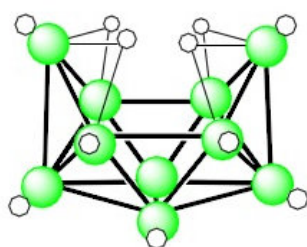
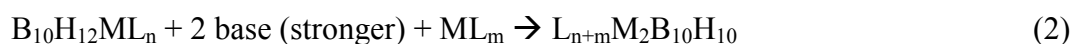
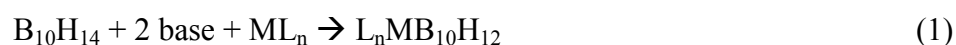


**Figure 1. 7.** The molecular structure of *nido*-decaborane.

The high molecular boron content and stability of decaborane (or larger clusters such as  $B_{18}H_{22}$ ) makes them commercially interesting in the use as dopant agents in the manufacture of *p*-type semiconductor devices.<sup>68</sup>

The facile deprotonation of the decaborane cluster renders such species as excellent Lewis bases that readily react with metal-containing compounds to generate metallaboranes.<sup>69</sup> It is the intention of the work described in the first part of this thesis to prepare new metallaborane cluster systems.

The main synthetic strategy has two steps:



### 1. 8. 1. *nido*-7-metallaundecaboranes as dimetallaborane precursors

The structures of the 11-vertex transition metal *nido*-7-metallaundecaboranes (**Figure 1. 8.**) obtained from synthesis method (1) may generally be regarded as analogous to the  $[B_{11}H_{13}]^{2-}$  anion with two bridging hydrogen atoms being replaced by a { $ML_n$ } moiety, and two bridging hydrogen atoms remaining on the open-face of the cluster. The metal center contributes three orbitals to the bonding scheme of the { $MB_{10}H_{12}$ } cluster. [*nido*- $L_nMB_{10}H_{12}$ ] derivatives are known for Cr, Mo, W, Co, Rh, Ru, Ir, Ni and Pd.<sup>69</sup> Particularly well presented are platinum derivatives, which are important for this thesis.<sup>65,70</sup>

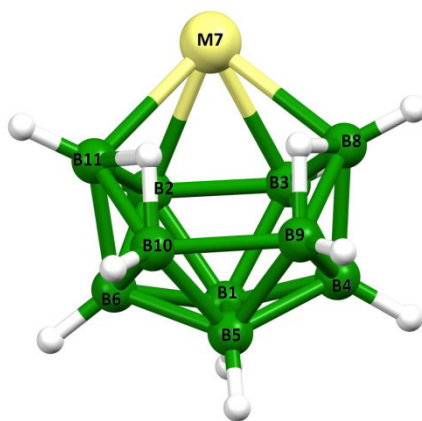


**Figure 1. 8.** General structure of *nido*-7-metallaundecaboranes (metal ligands external to the boron cluster have been omitted for reasons of clarity).

Theoretically straightforward syntheses based on halide displacement from metal centres by the *nido*-decaboranyl anion works in general only for platinum species.<sup>70</sup> In the cases of other transition metals, cluster degradation occurs to give 10-vertex *nido*-5- or *nido*-6-metalladecaboranes (Rh, Ru).<sup>69</sup> Weaker ligands can be also displaced to yield *bis*-decaboranyl  $[\text{B}_{10}\text{H}_{12}\text{-M-B}_{10}\text{H}_{12}]^{2-}$  sandwich molecules (Pd, Ni, Co).<sup>71</sup> One of the possible ways (that was also used during this work) how to avoid these processes is to use methylated metal complexes of type  $[\text{ML}_n(\text{Me})_2]$ , that avoid the necessity of a base to remove two bridging hydrogen atoms from the borane cluster - the only side product of the reaction being methane gas.

Platinum, nickel and palladium derivatives have been studied extensively, particularly those with two  $\text{PR}_3$  phosphine ligands on the metal center.<sup>70</sup> These compounds are mostly air stable yellow solids. The structural type of these species is exemplified by the compound  $[(\text{PMe}_2\text{Ph})_2\text{PtB}_{10}\text{H}_{12}]$ : The observed platinum-to-borane cluster binding geometry is formally derived by the replacement of two B-H-B bridging bonds with two B-Pt-B three center bond combined with square planar 16-electron  $d^8$  Pt(II) behavior. The Pt-P vectors are mutually in *trans* positions, which is consistent with the above assignment.<sup>69</sup>

Other main-group metal derivatives are also known. They have in general two-orbital contribution to the cluster bonding, and are therefore best described as electronic and structural analogous of the  $[\text{B}_{11}\text{H}_{14}]^-$  anion. Most of these compounds can be regarded as *tetrahapto* bidentate complexes and are known for Mg, Zn, Cd, Hg, Al, Ga, In, Th, Si, Ge and Sn.<sup>69</sup>

### 1. 8. 2. *closo* 1,2-dimetalladodecaboranes

12-vertex *closo*-1,2-dimetalladodecaboranes (**Figure 1. 9.**) are known for Pt-Pt, Pt-Pd, Pd-Pd, Co-Ni and Ni-Ni. These species may be considered as complexes between *nido*-7-metallaundecaborane ligands and metal centers.<sup>69</sup>

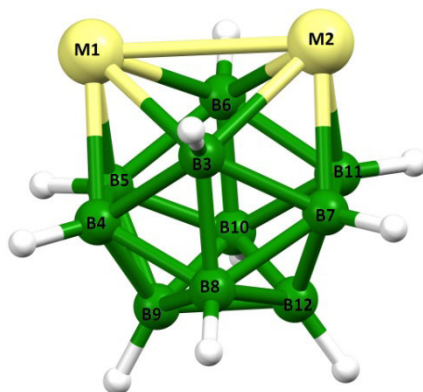


**Figure 1. 9.** General structure of *closo* 1,2-dimetalladodecaboranes (metal ligands external to the boron cluster have been omitted for reasons of clarity).

This thesis is focused mostly on diplatinum, dipalladium and platinum-palladium *nido*-decaborane derivatives. Other bimetallic species did not find any potential use so far. The first diplatinum compound [(PMe<sub>2</sub>Ph)<sub>4</sub>Pt<sub>2</sub>B<sub>10</sub>H<sub>10</sub>] was successfully synthesized in 1985 as a poorly soluble purple solid.<sup>72</sup> The great breakthrough was made at the beginning of a new millenium when it was found that this particular molecule has the propensity to reversible bind atmospheric oxygen across the dimetal vector of the cluster.<sup>73</sup> The cluster with and without bound dioxygen has significantly different stabilities: {Pt-O<sub>2</sub>-Pt(B<sub>10</sub>H<sub>10</sub>)} is stable only over 12 h in solution and several days in solid form; {Pt-Pt(B<sub>10</sub>H<sub>10</sub>)} remains stable over a period of decades (20 years-old samples was found, analyzed and no decomposition was observed).<sup>65</sup> This discovery caused a new intensive interest in metallaboranes that generally incorporate redoxflexible transition-element centres. There is only one previously reported metal-metal-bonded system for which dioxygen coordination has been reported - [Ir<sub>2</sub>I<sub>2</sub>(CO)<sub>2</sub>(O<sub>2</sub>)(Ph<sub>2</sub>PCH<sub>2</sub>PPh<sub>2</sub>)<sub>2</sub>] (**Figure 1. 10.**). However, the process is in this case irreversible.<sup>74</sup>

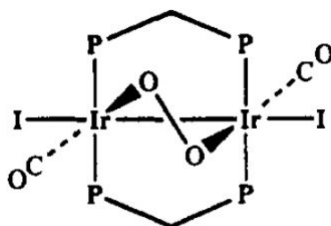


**Figure 1. 10.** The structure of the non borane system irreversibly sequestering O<sub>2</sub>.<sup>74</sup>

The dioxygen addition can be readily reversed upon gentle heating, by removal of solvent and volatiles under reduced pressure, or by purging with an inert gas such as argon or dinitrogen. The release and rebinding of the gas molecule can be also cycled *via* irradiation with UV light, though with a little photodegradation of the compound. Additionally, when captured dioxygen molecules are released *via* irradiation with UV light (the experiment is shown on **Figure 1. 11.**), some of this energy is transferred to the oxygen molecules that become electronically excited to singlet states (although in a very low quantum yield,  $\Phi < 0.01$ ).<sup>65,73</sup>

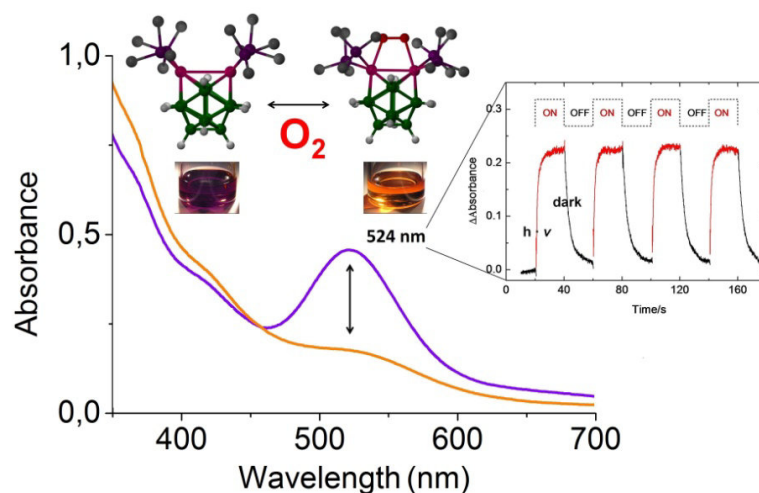


**Figure 1. 11.** UV/vis spectra before (purple) and after (orange) addition of dioxygen. Inset graph demonstrates the dependency of the uptake and release of dioxygen on the irradiation of UV light.

The structures of  $[(\text{PMe}_2\text{Ph})_4\text{Pt}_2]\text{B}_{10}\text{H}_{10}$  and  $[(\text{PMe}_2\text{Ph})_2\text{Pt}-\text{O}_2-\text{Pt}(\text{PMe}_2\text{Ph})_2]\text{B}_{10}\text{H}_{10}$  have small differences; (a) a concomitant shortening of Pt-Pt distance ( $2.95 \text{ \AA} \rightarrow 2.71 \text{ \AA}$ ), and (b) a flexing of the phosphine ligand sphere.  $\{(\text{PMe}_2\text{Ph})_4\}$  opens up with the P-organyl groups twisting out of the way to adapt for the attachment of the dioxygen molecule.<sup>73</sup> The interoxygen distance is longer than that in molecular oxygen ( $1.21 \rightarrow 1.43 \text{ \AA}$ ). It is analogous to the bond distance in peroxide ions or hydrogen peroxide ( $\approx 1.48 \text{ \AA}$ ), and longer than found in the dioxide anion ( $\approx 1.28 \text{ \AA}$ ). With the observation of the Pt-O-O-Pt torsion angle of  $15.8^\circ$ , a peroxide-like comparative description is preferable.<sup>75</sup>

The reversible uptake of several other gases were investigated and positive results were obtained with  $\text{SO}_2$  and  $\text{CO}$ . The important facts are that (a) whole processes are quantitative and (b) are accompanied by clear colour changes (**Figure 1. 12.**).

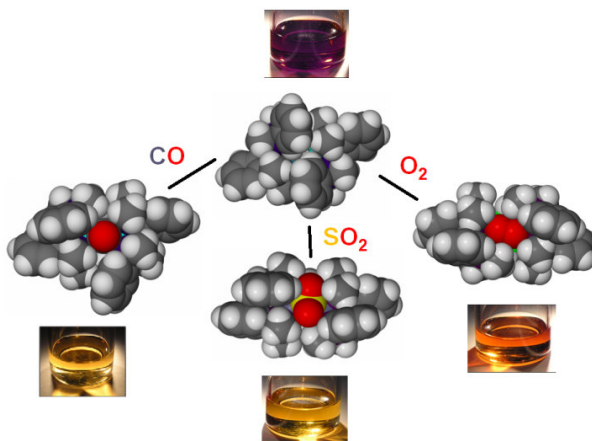


**Figure 1. 12.** Space-filling representations of the crystallographically determined molecular structures and solution colours of adducts with different bound gases.

In addition to the direct sequestering of CO and SO<sub>2</sub> by the bimetallic cluster, both gases can displace O<sub>2</sub> on the Pt-Pt center in an analogous way to how CO can displace O<sub>2</sub> bound to haem. In contrast to dioxygen binding, the additions of SO<sub>2</sub> and CO are not reversible under normal conditions of mild heating or pressure reduction, but require instead UV light irradiation.<sup>65</sup> Other examples of SO<sub>2</sub> (*e. g.* pentaplatinum cluster species - [Pt<sub>5</sub>(μ-SO<sub>2</sub>)<sub>3</sub>(CNC<sub>8</sub>H<sub>9</sub>)<sub>7</sub>])<sup>76</sup> or CO (*e. g.* carbonyl bridged diplatinum cationic species - [Pt<sub>2</sub>(μ-CO,μ-H)(dpe)<sub>2</sub>][BF<sub>4</sub>])<sup>77</sup> reversible sequestering on non-borane metallic compounds may be found in the literature, but rarely in combination with dioxygen binding. [Ir<sub>2</sub>I<sub>2</sub>(CO)<sub>2</sub>(O<sub>2</sub>)(Ph<sub>2</sub>PCH<sub>2</sub>PPh<sub>2</sub>)<sub>2</sub>] has the ability to react with CO and SO<sub>2</sub>, not to displace dioxygen but to generate the unusual species [Ir<sub>2</sub>I<sub>2</sub>(CO)<sub>2</sub>(CO<sub>3</sub>)(Ph<sub>2</sub>PCH<sub>2</sub>CH<sub>2</sub>PPh<sub>2</sub>)<sub>2</sub>] and [Ir<sub>2</sub>I<sub>2</sub>(CO)<sub>2</sub>(SO<sub>4</sub>)(Ph<sub>2</sub>PCH<sub>2</sub>CH<sub>2</sub>PPh<sub>2</sub>)<sub>2</sub>].<sup>73</sup>

The series of metallaboranes containing two adjacent metal atoms, [(PMe<sub>2</sub>Ph)<sub>4</sub>M-MB<sub>10</sub>H<sub>10</sub>] (M-M = Pt<sub>2</sub>; Pt-Pd; Pd<sub>2</sub>), have been synthesized previously, and their propensity to sequester O<sub>2</sub>, CO, and SO<sub>2</sub> and to then release them under pulsed and continuous UV irradiation was comprehensively described.<sup>65</sup> Of the bimetallic boron clusters ever reported, only Pt<sub>2</sub> binds dioxygen, which is the reason, why this compound was synthesized in good quantities for purposes for this project. The molecules of SO<sub>2</sub> and CO are bound more weakly in the sequence {PtPt} > {PtPd} > {PdPd}. This effect is caused by shortening metal-metal bond and thus weakening of metal-gas bonds.<sup>65</sup>

The above detailed properties of bimetallic borane cluster systems allude to their high potential for their use as sensors or as handy sources of bound gases. Moreover, the described system, [(PMe<sub>2</sub>Ph)<sub>4</sub>Pt<sub>2</sub>]B<sub>10</sub>H<sub>10</sub>, might conceivably have the propensity to bind other gaseous

molecules (for example, NO and NO<sub>2</sub>). Indeed, NO sequestration was investigated in the scope of this work.

We anticipate that the reversible capturing of NO by bimetallic borane clusters can be utilized for NO detection. Many current detection methods rely on irreversible NO reactions, thereby only allowing for observation of cumulative NO production, rather than real-time concentration changes. A system that could react with NO reversibly would allow for direct detection of both increases and decreases in NO concentrations, a currently unmet need in NO sensing.

The previously mentioned compound - [Ir<sub>2</sub>I<sub>2</sub>(CO)<sub>2</sub>(Ph<sub>2</sub>PCH<sub>2</sub>PPh<sub>2</sub>)<sub>2</sub>] (**Figure 1. 10.**) possesses the propensity to bind NO, however it does so irreversibly, as is the case for dioxygen and other gaseous molecules.<sup>74</sup> The propensity to reversibly bind NO can be found with haem complexes. In 2012 a study was published recording the reversible binding of nitric oxide to a non-haem Fe(III) complex of a tetra-amidomacrocyclic.<sup>78</sup> This complex binds NO with a 1 : 1 stoichiometry and upon purging with nitrogen, the coordinated NO is released to regenerate the parent Fe(III) complex (**Figure 1. 13.**)<sup>78</sup>

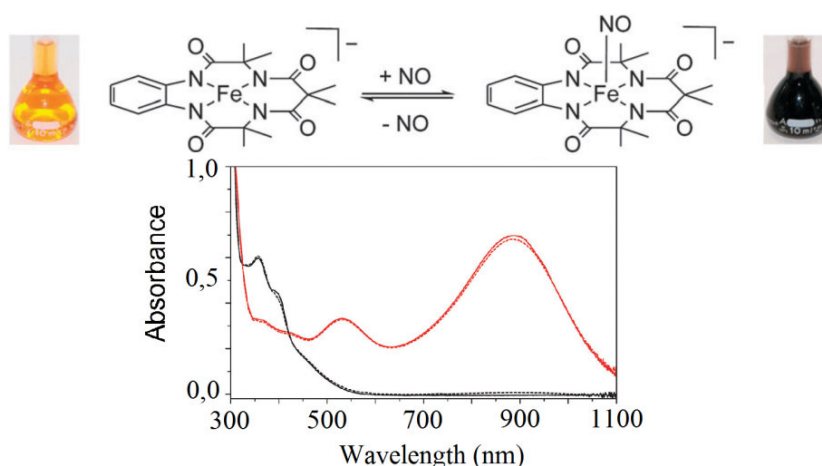


**Figure 1. 13.** Reversible binding of NO to Fe(III) complexes. UV/vis spectra before (black) and after (red) addition of NO.<sup>78</sup>

Many similar systems can release NO upon its photolysis - for example the photolabile NO complexes of manganese, ruthenium or iron (**Chapter 1. 7.**)<sup>54</sup>

### 1. 9. NO detection methods

One of the methods for the indirect identification of NO is the Griess reaction. It is a two-step diazotization reaction in which dinitrogen trioxide (N<sub>2</sub>O<sub>3</sub>) generated from the acid-catalyzed autoxidation of NO reacts with sulfanilamide to produce a diazonium ion which is

then coupled to N-(1-naphthyl)ethylenediamine to form a chromophoric azo product that absorbs strongly at 540 nm.<sup>79</sup>

Increased sensitivity in NO detection (10-30 nM) is achieved by using fluorometric methods. The relatively nonfluorescent 2,3-diaminonaphthalene (DAN) reacts rapidly with  $N_2O_3$  generated from the interaction of NO with oxygen to yield the highly fluorescent product 2,3-naphthotriazole (NAT) as seen in **Figure 1. 14**.

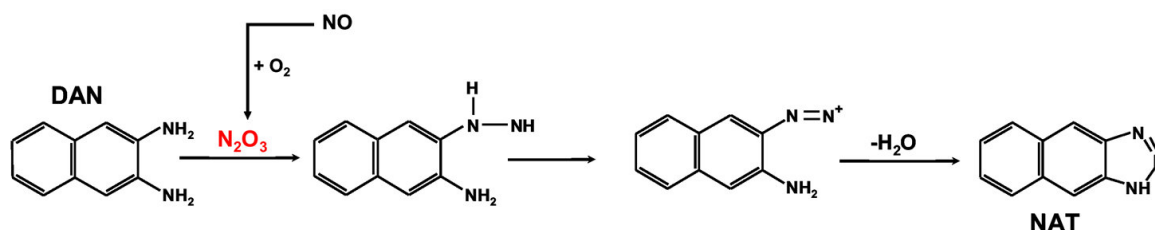


**Figure 1. 14.** Fluorometric detection of NO using diaminonaphthalene (DAN) assay.

Using myoglobin (Mb) is a simple and fast way to qualitatively detect NO. Mb exhibits its Soret band at 410 nm. Reduction with dithionite results in a shift of the absorption maximum to 432 nm. Subsequent reaction with NO leads in the appearance of a new Soret band at 420 nm.<sup>80</sup>

The most commonly employed direct NO measurement technique is amperometric detection. Advantages are short response time and sensitivity  $>1$  nM. Generated NO diffuses across the gas permeable/NO-selective membrane and is oxidized at the working electrode surface producing a redox current. The amount of NO oxidized is proportional to the current flow between working and reference electrodes, which is measured by an NO meter.<sup>81</sup>

### 1. 10. Materials simultaneously photoreleasing $O_2(^1\Delta_g)$ and NO

The use of more active species in conjunction is highly desirable for an effective action. Suitable highly reactive species that can be used in combination are singlet oxygen and nitric oxide due their ready photogeneration and characteristic properties described previously.

The first molecular system able to deliver simultaneously NO and  $O_2(^1\Delta_g)$ , in the same region of space, and under the control of a daylight was prepared in 2007 (**Figure 1. 15**).<sup>82</sup> Synthesis of this multifunctional micellar nanoassembly formed by the mesogen-bearing cationic amphiphilic NO-photodonor and the anionic porphyrin is based on favorable electrostatic interactions. The strong fluorescence and reduced size make it an appealing candidate to be tested in biological research. However, the efficiency of photogeneration of NO is very low  $\Phi \approx 0.01$ .<sup>82</sup>

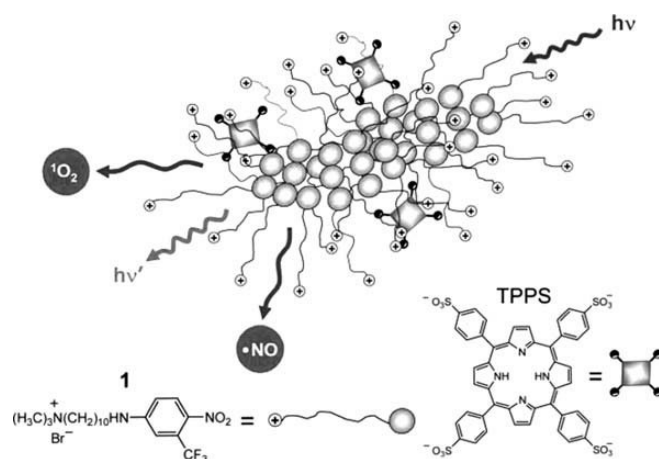


**Figure 1. 15.** Idealized view of the multifunctional micellar nanoassembly.<sup>82</sup>

Another similar systems are multilayer films on quartz substrates that are composed of tetrasulfonated porphyrins and cationic amphiphilic NO-photodonors.<sup>83</sup>

Nitrosyl ruthenium complex conjugated with a phthalocyanine rare earth complex is a molecular system capable of nitric oxide and singlet oxygen photo-generation by light irradiation.<sup>84</sup> Although the solutions of this self-assembly strongly inhibits the cell viability in a light irradiation-dependent manner, disadvantage lies in its high complexity (**Figure 1. 16.**) and difficult characterization.

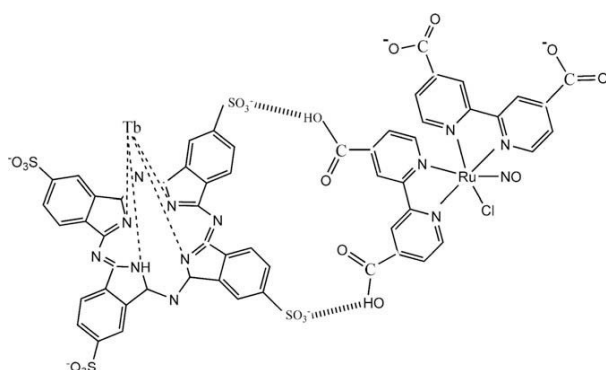


**Figure 1. 16.** Illustration of the nitrosyl ruthenium and rare earth complex self-assembly.<sup>84</sup>

On the other hand, nitrosyl ruthenium phthalocyanin complex itself is less complex and easier to obtain (**Figure 1. 17.**)<sup>85</sup> The complex was prepared by bubbling NO through an ethanolic solution containing ruthenium phthalocyanin. The synergistic effect of photogenerated NO and singlet oxygen was confirmed and the antiproliferative activity on cell culture may provide this compound for using in cancer treatment. However, the efficiency of NO and  $O_2(^1\Delta_g)$  generation is low.



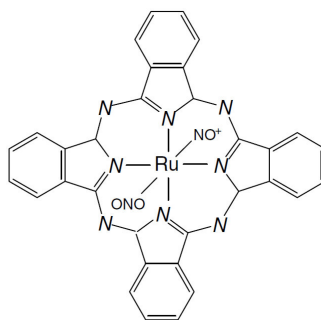


**Figure 1. 17.** Illustration of the nitrosyl ruthenium complex.

TiO<sub>2</sub> nanotubes modified with NO-photodonor (S-Nitrosocysteine) and PbS quantum dots<sup>86</sup> have also been employed for photogeneration of nitric oxide and singlet oxygen. Nevertheless, this system requires near infrared excitation wavelength. Moreover, lead(II) sulfide is rather toxic thus this system is not very suitable for medicinal use.

To our best knowledge, studies dealing with multifunctional nanofiber materials photogenerating simultaneously NO and O<sub>2</sub>(<sup>1</sup>Δ<sub>g</sub>), have not been published yet.

## 2. The aims of the study

The objective of this study was:

- I. to prepare and investigate new nanofiber materials with covalently bonded NO-photodonor and ionically-bound tetracationic porphyrinoid photosensitizers (**Figure 2. 1.**) on the surface of polystyrene (PS) electrospun nanofiber materials. These bonded photoactive compounds enable efficient simultaneous photogeneration of  $O_2(^1\Delta_g)$  and NO species triggered by visible light.
- II. to investigate reversible binding of NO on the bimetalaborane cluster system for purposes of its short-time storage and detection, this task include the preparation of new mono-metallic precursors and subsequently new bimetalaborane species with the propensity to reversibly sequester small gaseous molecules.

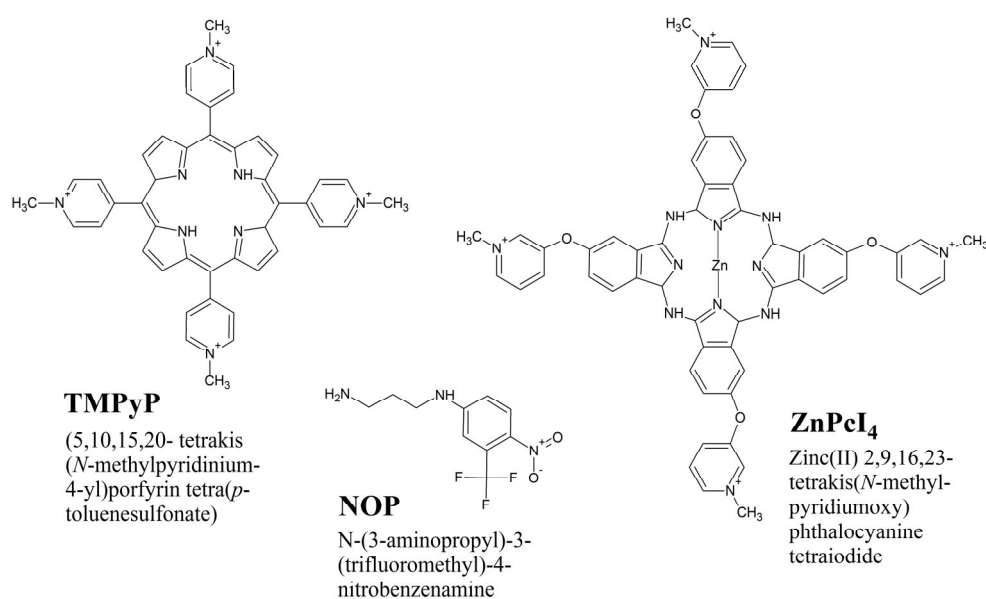


**Figure 2. 1.** Chemical structures of compounds used for nanofiber modification.

## 3. Experimental section

### 3. 1. Chemicals and materials

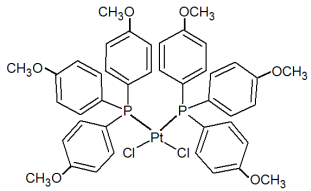
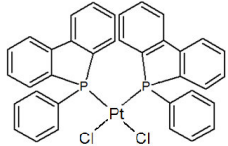
Polystyrene Synthos PS GP 137 was purchased from Synthos Kralupy a.s., Czech Republic. Zinc(II) 2,9,16,23-tetrakis(*N*-methyl-pyridiumoxy)phthalocyanine tetraiodide (ZnPcI<sub>4</sub>) was purchased from COC s.r.o., Rybitví and used as received. *nido*-B<sub>10</sub>H<sub>14</sub> was obtained commercially (Katchem, Prague) and sublimed before used. Dichloromethane and toluene (Fluka) were dried over appropriate desiccants and stored in 500 mL RB flasks fitted with Teflon vacuum taps and transferred by vacuum distillation into vessels cooled by liquid N<sub>2</sub>. Other chemicals, such as solvents, deprotonation agents and starting materials were bought at reagent or analytical grade from Sigma Aldrich and were used as purchased. NO-photodonor *N*-(3-aminopropyl)-3-(trifluoromethyl)-4-nitrobenzenamine (NOP) was synthesized and characterized in accordance with literature.<sup>87</sup> [(PMe<sub>2</sub>Ph)<sub>4</sub>Pt<sub>2</sub>B<sub>10</sub>H<sub>10</sub>] was prepared and purified for NO capture investigation using the published procedure.<sup>65</sup>

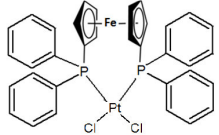
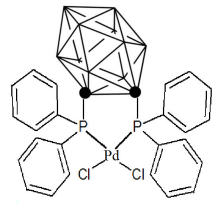
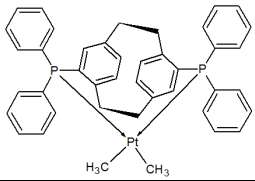
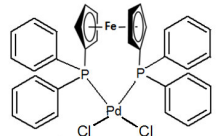
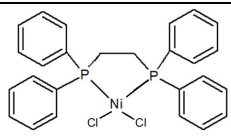
### 3. 2. General synthetic procedures

The syntheses of all metallaborane species were carried out using standard vacuum or inert-atmosphere techniques, although subsequent operations were generally carried out in air, except for a number of those involving solutions of the oxygen-sensitive [(PMe<sub>2</sub>Ph)<sub>4</sub>Pt<sub>2</sub>B<sub>10</sub>H<sub>10</sub>]. Other syntheses (preparation of metallophosphine complexes *etc.*) were carried out in air.

Metallophosphine precursors **MP1** - **5** were synthesized and characterized in accordance to literature (individual references given in **Table 3. 1.**). **MP6** and **MP7** were purchased from Sigma Aldrich and used as received.

**Table 3. 1.** Names and structures of used metallophosphines.

Abbreviation	Chemical Name	Structure
<b>MP1</b>	Bis(tris(4-methoxyphenyl)phosphine)dichloro platinum(II) <sup>88</sup>	
<b>MP2</b>	Bis(5-phenyl-5h-benzo[ <i>b</i> ]phosphindole)dichloro platinum(II) <sup>89,90</sup>	

<b>MP3</b>	[1,1'-Bis(diphenylphosphino)ferrocene]dichloro platinum(II) <sup>91</sup>	
<b>MP4</b>	[1,1'-Bis(diphenylphosphino)oc-carborane] dichloropalladium(II) <sup>92</sup>	
<b>MP5</b>	(S)-(+)-4,12-Bis(diphenylphosphino)-[2.2]-paracyclophane)dimethylplatinum(II) <sup>93</sup>	
<b>MP6</b>	[1,1'-Bis(diphenylphosphino)ferrocene]dichloro palladium(II)	
<b>MP7</b>	[1,1'-Bis(diphenylphosphino)ethane]dichloro nickel(II)	

### Synthesis of monometallaboranes M1 - 4 and M6

(numbering corresponds with metallaphosphine ligands, e. g. MP1 → M1)

In a typical experiment, *nido*-B<sub>10</sub>H<sub>14</sub> (0.042 g; 0.34 mmol), bdmn (147 mg; 0.68 mmol) and the relevant metallaphosphine complex (0.331 g of **MP1**; 0.258 g of **MP2**; 0.265 g of **MP3**; 0.235 g of **MP4**; 0.250 g of **MP6**; all 0.34 mmol) were placed together (1:2:1 ratio) into a 100 ml two-necked round-bottomed flask under a stream of inert argon gas, and attached to a high-vacuum line. Dry dichloromethane (*ca.* 50 ml) was subsequently condensed under vacuum into the flask and the mixture was allowed to warm to room temperature whilst stirring. Small aliquots were taken at several intervals during the course of the reaction for examination by <sup>11</sup>B, <sup>1</sup>H and <sup>31</sup>P NMR spectroscopy. Once the <sup>11</sup>B NMR spectra indicated a completion of reaction, or at least an equilibrium between starting material and product, (usually after 24 hours) the reaction mixture was filtered. Subsequent flash column chromatography (dichloromethane:*n*-hexane; 9:1) of the filtrate was performed until the fastest band was eluted and collected. Then the volume of the elute was reduced and layered with *n*-hexane. Overnight crystals suitable for single-crystal X-ray analysis formed and were filtered, washed with *n*-hexane and dried under vacuum.

### Synthesis of monometallaborane M5

The methylation of (S)-(+)-4,12-Bis(diphenylphosphino)-[2.2]-paracyclophane) dichloroplatinum(II) was performed as follows: (S)-(+)-4,12-Bis(diphenylphosphino)-[2.2]-paracyclophane)dichloroplatinum(II) (0.5 g; 0.595 mmol) was stirred in toluene (40 ml) at -70°C in a two-necked round-bottomed flask attached to a high-vacuum line and 2.5 equivalents of MeLi (1.6 M in diethylether; 2.4 ml; 1.49 mmol) were added. The reaction mixture was slowly allowed to warm to ambient temperature and then cooled in an icewater bath and distilled H<sub>2</sub>O (20 ml) was added to get rid of any excess MeLi. The solution was then reduced to dryness, the solid product was subsequently dissolved in dichloromethane, layered with *n*-hexane and left crystallize in the fridge. Next day, crystals were filtered, washed with *n*-hexane and air-dried, yielding 90% of **MP5**.

**MP5** (0.25 g; 0.313 mmol) and *nido*-B<sub>10</sub>H<sub>14</sub> (0.038 g; 0.313 mmol) were placed into a clean 100 ml round-bottomed flask with a stir bar. This flask was then evacuated of air and *ca.* 40 ml of dichloromethane was condensed into the flask and stirring begun. After warming up to ambient temperature the reaction mixture slowly became a deep yellow. This mixture in the flask was stirred overnight. After 14 hours of stirring the <sup>11</sup>B, <sup>1</sup>H and <sup>31</sup>P NMR spectra showed one pure asymmetric monometallic product. So the volume of the mixture was reduced and carefully layered with *n*-hexane. The next day crystals were filtered and dried under vacuum in the dessication jar.

### Synthesis of monometallaborane M7

*nido*-B<sub>10</sub>H<sub>14</sub> (0.069 g; 0.566 mmol) was placed into a 100 ml three-necked round-bottomed flask, that was attached to a high-vacuum line. Dry diethylether (*ca.* 50 ml) was condensed under vacuum into the flask. Immediately the apparatus was flushed with a positive pressure of argon gas and then two equivalents (1.2 ml; 1.2 mmol) of KHBET<sub>3</sub> (1M in tetrahydrofuran) were injected through a suba-sealed sidearm. On addition, the mixture slowly became cloudy. After warming up to ambient temperature one equivalent of **MP7** (0.301 g; 0.566 mmol) was added *via* a tipper tube, resulting in the formation of an orange-brown precipitate. After two hours the precipitate was filtered, washed with diethylether and dried under vacuum. Subsequent column chromatography (dichloromethane:*n*-hexane; 9:1) of the orange-brown powder, collection of an orange-brown elute, reduction in its volume and layering with *n*-hexane led to the growth of crystals suitable for single-crystal X-ray analysis that were filtered, washed with hexane and dried under vacuum.

### 3. 3. Electrospinning

A mixture of 0.07 wt % TEAB, and 99.93 wt % polystyrene (PS) were dissolved in cyclohexanone to prepare a 17% solution for the fabrication of PS nanofiber material. The nanofiber materials were produced using the modified Nanospider™ electrospinning industrial technology. This used simultaneous formation of charged liquid jets on the surface of a thin wire electrode, where the locations of the jets are set up naturally in their optimal positions.

### 3. 4. Scanning Electron Microscopy (SEM)

The nanofiber morphology was studied with a scanning electron Quanta 200 FEG microscope (FEI, Czech Republic).

### 3. 5. Ion exchange capacity (IEC) with adsorption kinetics

Approximately 100 cm<sup>2</sup> of the sulfonated material was treated with 20 ml of 10 mM NaOH solution for 1 day to exchange the H<sup>+</sup> with Na<sup>+</sup>. Remaining NaOH was titrated by 10 mM HCl using potentiometric indication. IEC was related to the mass of dried materials.

The same procedure was also employed for aminated material N1. From the IEC the quantity of bonded compounds on the surface was calculated.

### 3. 6. Fourier transform infrared spectra (FTIR)

The functional groups on PS surface before and after derivatization were studied using Fourier Transform Infrared spectroscopy (FTIR). Infrared absorption spectra were measured with a Thermo Nicolet 8700 FTIR spectrometer by attenuated total reflectance (ATR) setup using Specac's Gateway™ 6-reflection horizontal ATR accessory with ZnSe ATR prism. The ATR method was applied using IR source, KBr beam-splitter and liquid nitrogen cooled photodiode (MCT) as a detector. A background spectrum was recorded using clean ZnSe ATR prism without PS. During the IR measurements the PS were kept in a N<sub>2</sub> purged chamber of the FTIR spectrometer. The advanced ATR correction was applied on the measured spectra.

### 3. 7. UV/vis absorption and fluorescence spectroscopy

The UV/vis absorption spectra were recorded using Unicam 340 and Varian 4000 spectrometers. The steady-state fluorescence spectra were monitored using a Aminco Bowman (AB2) spectrometer.

### 3. 8. Photooxidation of model species by nanofiber materials

A piece of the nanofiber material was placed in a thermostatted 10 mm quartz cell (22 °C) containing  $2 \times 10^{-4}$  M of uric acid in 0.02 M of phosphate buffer (pH = 7.0) or 0.1 M of iodide detection solution. The cell was irradiated with visible light from a stabilized xenon lamp (500 W, Newport) with a long-pass filter ( $\lambda \geq 400$  nm, Newport). The UV/vis absorbance changes at 292 nm (attributed to photodegradation of uric acid) or at 351 nm (attributed to the formation of  $I_3^-$  in iodide test), were recorded and compared to a blank solution of the same composition that was stored in the dark.

### 3. 9. Chemical detection of NO

Released NO was detected using DAN and myoglobin (Mb) chemical tests. The DAN test is based on the reaction of non-fluorescent 2,3-diaminonaphthalene (DAN) with  $N_2O_3$  which is immediately formed by reaction of NO with  $O_2$ . The reaction of DAN with  $N_2O_3$  yields the highly fluorescent 2,3-naphthotriazole. A piece of nanofiber materials (2 cm<sup>2</sup> on quartz plate) was placed in a thermostatted 10 mm quartz cell (22 °C) containing 3.5 ml of 0.31 mM DAN in 0.62 M HCl. The cell was irradiated with visible light from a stabilized xenon lamp (500 W, Newport) with a long pass filter ( $\lambda \geq 400$  nm, Newport). After the irradiation 200  $\mu$ l aliquot and 100  $\mu$ l 2.8 M NaOH was put into the fluorescent cuvette and diluted by 3.2 ml of distilled  $H_2O$ . NO was detected as an emission band at 450 nm ( $\lambda_{exc} = 365$  nm).

The Mb test is based on UV/vis detection of the Mb(Fe<sup>II</sup>)-NO adduct. The UV/vis spectra of 3.5 ml 3 mM Mb in phosphate buffer (pH = 7.0) before and after the addition of 250  $\mu$ l 0.05 M  $Na_2S_2O_4$  in  $H_2O$  were recorded. The reduction of Mb(Fe<sup>III</sup>) to Mb(Fe<sup>II</sup>) was observed as a shift of the Soret band from 410 to 432 nm. The piece of nanofiber materials (2 cm<sup>2</sup> on quartz plate) was added into thermostatted 10 mm quartz cell (22 °C) containing freshly prepared Mb(Fe<sup>II</sup>) detection solution. The cell was irradiated with visible light from a stabilized xenon lamp (500 W, Newport) with long pass filter ( $\lambda \geq 400$  nm, Newport). After the irradiation the Soret absorption band of NO-adduct at 420 nm was detected.

Alternatively, for photogeneration of nitric oxide 200 mW diode laser (iBeam Smart, Toptica Photonics, Germany,  $\lambda = 402$  nm) was used.

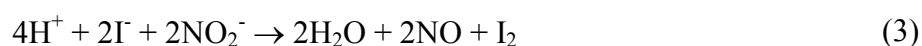
### 3. 10. The time-resolved near-infrared phosphorescence of $O_2(^1\Delta_g)$

The samples of PS nanofiber materials with photoactive compounds were placed on a quartz plate and immersed in an evacuable cell containing  $D_2O$ . The cell was connected to a glass vacuum line or to oxygen. Total pressure in the cell was measured with capacitance manometers (MKS Baratron). Samples were excited by a Lambda Physik COMPEX102 excimer

laser (308 nm, pulse width 28 ns) and an FL 3002 dye laser (425 nm, 658 nm). Time-resolved near-infrared phosphorescence of  $O_2(^1\Delta_g)$  at 1270 nm was observed at the right angle to an excitation pulse using a homemade detector unit (interference filter, Ge diode Judson J16-8SP-R05M-HS).

### 3. 11. Amperometric detection of NO

The release of NO was measured with a World Precision Instrument, ISO-NO meter, equipped with a data acquisition system, and based on direct amperometric detection of NO with short response time ( $< 5$  s) and sensitivity range 1 nM – 20  $\mu$ M. The analog signal was digitalized with a four-channel recording system and transferred to a computer. The sensor was accurately calibrated by mixing standard solutions of  $NaNO_2$  with 0.1 M  $H_2SO_4$  and 0.1 M KI according to the reaction:



A sample of nanofiber material was fixed on quartz plate and placed in a thermostated quartz cell ( $1 \times 1 \times 4$  cm) with  $H_2O$ . The irradiation was performed by 100mW laser (405 nm). During the irradiation the  $H_2O$  in cell was stirred. NO measurements were carried out using the electrode positioned outside the light path in order to avoid NO signal artifacts due to photoelectric interference on the ISO-NO electrode.

### 3. 12. Antibacterial tests

A culture of *Escherichia coli* DH5 $\alpha$  (Invitrogen, CA, USA) which was incubated with stirring in LB medium at 37°C. Incubation was stopped when the absorbance at 560 nm reached a value *ca.* 1. Thus prepared culture was diluted  $10^4$  to the desired concentration in PBS. The nanofiber materials (5  $cm^2$ , free or doped by NO-photodonor and photosensitizer) were placed in quartz cuvette containing 1 ml of the bacteria suspension and then irradiated with visible light from a stabilized xenon lamp (500 W, Newport) with long pass filter ( $\lambda \geq 400$  nm, Newport) for 5 or 10 minutes or stored in the dark. After short shaking, 300  $\mu$ l of bacterial suspensions was put on the sterile agar plates. The plates were incubated 12 hours in darkness at 37 °C to allow the individual bacteria to grow and form colonies. Colonies formation units (CFU) were counted.

### 3. 13. NMR Spectroscopy

Boron has two naturally occurring NMR active nuclei –  $^{10}B$  (20.1%) and  $^{11}B$  (79.9%).  $^{11}B$  has a spin of 3/2 and  $^{10}B$  is spin 3. For general purposes  $^{11}B$  is the more useful nucleus with regards to NMR spectroscopy as it has the lower quadrupole moment of the two isotopes and is more sensitive.<sup>94</sup>



$^1\text{H}$ ,  $^{11}\text{B}$  and  $^{31}\text{P}$  spectra were measured using a Varian Mercury 400 Plus spectrometer.  $^{11}\text{B}$  NMR spectra were measured at 128.3 MHz with an inner standard  $\text{F}_3\text{B}\cdot\text{OEt}_2$ .  $^1\text{H}$  NMR spectra were measured at 400 MHz with an inner standard  $\text{Me}_4\text{Si}$ .  $^{31}\text{P}$  NMR spectra were measured at 40.48 MHz with an inner standard aqueous  $\text{H}_3\text{PO}_4$  (nominally 85%). Chemical shifts are given in  $\delta$  [ppm] units relative to the standards. Coupling constants  $J$  are reported in Hz units.

### 3. 14. Chromatography

For thin-layer chromatography (TLC), silica gel plates Merck 60 F254 were used, and compounds were visualized with UV light or by development with iodine and aqueous silver nitrate solution. Preparative thin-layer chromatography (TLC) was carried out using 1 mm thick layers of silica gel G (Macherey-Nagel, type UV254) as the stationary phase, supported on glass plates of dimensions 20 cm  $\times$  20 cm, the assemblies being made in-house from water slurries followed by drying in air at 80°C. Flash column chromatography was performed by using silica gel Merck 60 (particle size 0.063–0.200 mm).

### 3. 15. Single-crystal X-ray Diffractometry

Collection of single-crystal X-ray diffraction data for molecular structure determination of **M1**, **3**, **4** and **6** was performed on a Nonius Kappa CCD diffractometer ( $\text{MoK}_\alpha$  radiation, graphite monochromator). The phase problem was solved utilizing direct methods in implementation of SIR-92 and the non-hydrogen atoms were refined anisotropically, using the full-matrix least-squares procedure taken from SHELXL-97. The positions of the hydrogen atoms were localised on difference Fourier maps and refined isotropically.

Diffraction data of **M2**, **5** and **7** were collected on four circle CCD diffractometer Rigaku MicroMax-007 HF with rotating anode ( $\text{MoK}_\alpha$  radiation, 120 K). For collection of diffraction data was used CrystalClear-SM Expert, for data reduction CrystalClear-SM Expert and XDS and for data processing SHELXTL, Mercury and Olex2.

### 3. 16. Software

Origin 9.0 was used for data processing. 2D chemical structures were drawn in Chem-Sketch 12.1, 3D structures were drawn in Mercury 8.1.

## 4. Results and discussion for Aim I

### 4. 1. Preparation, IEC and morphology of nanofiber materials

The first steps for the preparation of electrospun nanofiber materials enriched with photoactive compounds were made in an air-bag filled by N<sub>2</sub> to avoid sample contact with air humidity that could hydrolyze the –SO<sub>2</sub>Cl to –SO<sub>3</sub><sup>–</sup> functional groups and therefore reduce the reaction with amine groups of the NO-photodonor molecule.

An electrospun PS nanofiber material (60 cm<sup>2</sup>) was fixed on quartz substrates and immersed in a 85 ml HSO<sub>3</sub>Cl bath for 1 min at ambient temperature. This material was subsequently washed by CH<sub>2</sub>Cl<sub>2</sub> and immersed in a 100 ml solution of 3 mM NO-photodonor in CH<sub>2</sub>Cl<sub>2</sub> for 24 hours.

The NO-photodonor used here was synthesized and characterized in accordance to the literature<sup>87</sup> (**Figure 4. 1.**).

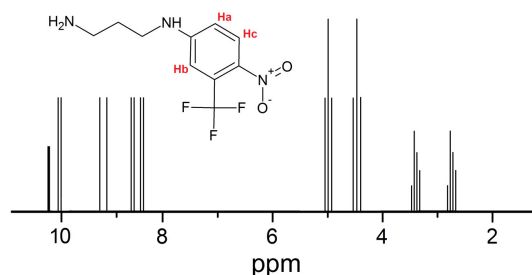


**Figure 4. 1.** Molecular structure and corresponding <sup>1</sup>H-NMR spectrum of NO-photodonor in CDCl<sub>3</sub>. <sup>1</sup>H-NMR CDCl<sub>3</sub>: δ 10.13 (1H, s broad, NH), 10.05 (1H, d, ArH<sub>a</sub>, J = 2,6 Hz), 9.20 (1H, d, J = 9.2 Hz, ArH<sub>c</sub>), 8.57 (1H, dd, J<sub>1</sub> = 9.2 Hz, J<sub>2</sub> = 2.6 Hz, ArH<sub>b</sub>), 5.02 (2H, t, J = 7.1 Hz, NH<sub>2</sub>CH<sub>2</sub>CH<sub>2</sub>CH<sub>2</sub>NH), 4.51 (2H, t, J = 7.2 Hz, NH<sub>2</sub>CH<sub>2</sub>CH<sub>2</sub>CH<sub>2</sub>NH), 3.47 (2H, m, NH<sub>2</sub>CH<sub>2</sub>CH<sub>2</sub>CH<sub>2</sub>NH), 2.8 (2H, m, NH<sub>2</sub>).

The structurally similar and commercially available NO-photodonor 4-Nitro-3-(trifluoromethyl)aniline exhibits an absorption maximum at 380 nm. Synthesized NOP better meets our demands as its absorption peak is shifted to 400 nm, and as such is active under visible light.<sup>87</sup>

The chlorosulfonated polystyrene was removed from its air-bag, washed by CH<sub>2</sub>Cl<sub>2</sub> and allowed to dry in air (12 hours) where unreacted –SO<sub>2</sub>Cl groups on the surface of material are gently hydrolyzed to –SO<sub>3</sub><sup>–</sup> groups by air humidity. The dry material was then neutralized using a 0.02M phosphate buffer (pH = 7.0), washed by H<sub>2</sub>O and put into 20 ml loading aqueous solution of 10<sup>–3</sup>M TMPyP or 10<sup>–3</sup>M ZnPcI<sub>4</sub> for 12 hours during which time free –SO<sub>3</sub><sup>–</sup> groups form ion-pairs with tetracationic photosensitizers.

TMPyP is a tetracationic porphyrin that has been studied as a dye for use in photodynamic therapy (PDT)<sup>95</sup> It is an efficient photosensitizer of singlet oxygen ( $\Phi = 0.74$  in wa-

ter).<sup>96</sup>  $\text{ZnPcI}_4$  is a tetracationic phthalocyanin compound. Phthalocyanines are also important photosensitizers used in PDT.<sup>95</sup> This particular phthalocyanin possesses the quantum yield of singlet oxygen production  $\Phi = 0.58$  in dimethylformamide.<sup>97</sup> A strong aggregation occurs when is dissolved in water and quantum yield drops almost to zero.

This procedure facilitates reaction control and enables an estimation to be made of the quantity of bonded NO-photodonor (NOP) simply by terms of the concentration of the loading solution, which unable NOP to interact with all  $-\text{SO}_2\text{Cl}$  groups. That opens the way to the ionic attachment of the next cationic photoactive compound to the hydrolyzed anionic  $-\text{SO}_3^-$  groups.

Three types of electrospun polystyrene nanofiber materials, assigned as **N1**, **N2**, **N3**, with externally bonded photoactive compounds were prepared and studied. Materials

- with covalently bonded NO-photodonor (**N1**)
- with covalently bonded NO-photodonor and ionically attached TMPyP (**N2**)
- with covalently bonded NO-photodonor and ionically attached  $\text{ZnPcI}_4$  (**N3**)

As follows from the **Figure 4. 2.**, the chlorsulfonation and subsequent binding of photoactive compounds slightly increased the average diameter of the PS nanofibers. Nevertheless, it is evident that the nanofibrous character of the PS material remains even after surface derivatization.

The colour changes caused by surface modification can serve as a first indication of the succesful bonding of the photoactive molecules (**Figure 4. 2.**): bright yellow for **N1**, dark brown for **N2**, blue-green for **N3**.

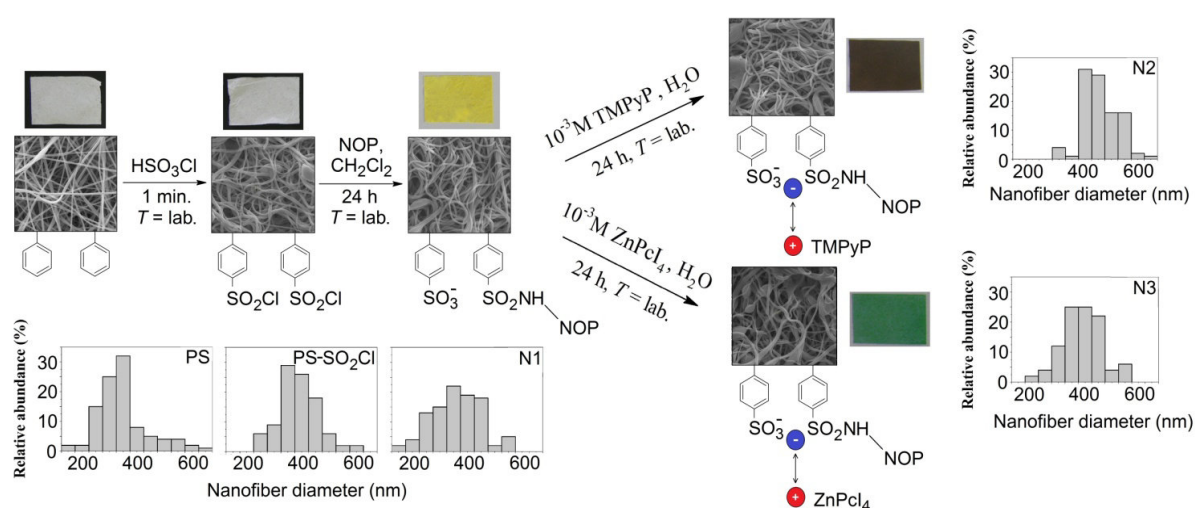


**Figure 4. 2.** Reaction scheme, corresponding SEM (with distribution of nanofiber diamaters) and images of PS nanofiber electrospun materials before and after the attachment of photoactive compounds.

In contrast to pure PS, which is a highly hydrophobic material, the functionalized materials **N1**, **N2** and **N3** are all highly hydrophilic. The increased wettability can be characterized by water droplet contact angles; PS nanofibers:  $130\pm 4^\circ$ ; **N1**, **N2** and **N3**:  $\leq 5^\circ$  (**Figure 4.3**). Recently, it was found that the increased wettability of the surface of material generating short-living species with short diffusion pathway (as  $O_2(^1\Delta_g)$ ) is a crucial factor for their efficient surface reaction with a substrate/biological target in aqueous environment.<sup>98</sup>

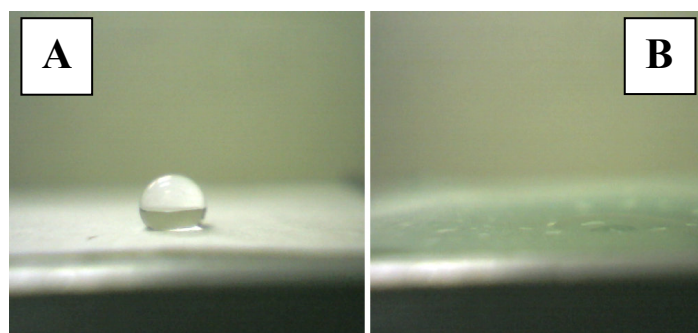


**Figure 4.3.** Contact angles measurement with pristine PS (A) and **N3** (B).

The high ion-exchange capacity (IEC) of chlorosulfonated and hydrolyzed PS nanofiber materials was observed ( $IEC = 2.5 \text{ mmol g}^{-1}$ ) in agreement with a previous study. The IEC of sulfonated PS materials is considerably suppressed after modification with NOP ( $IEC = 0.85 \text{ mmol g}^{-1}$ ). From the difference in IEC (before and after the derivatization) we can calculate that material **N1** has  $1.65 \text{ mmol g}^{-1}$  ( $0.29 \text{ mg/1cm}^2$ ) bonded NO-photodonor molecules to the nanofiber material.

The **Figure 4.4** shows the kinetics of adsorption of  $10^{-3}\text{M}$  TMPyP and  $10^{-3}\text{M}$   $ZnPcI_4$  from aqueous solutions to the surface of sulphonated PS nanofiber materials both with and without NO-photodonor modification. The adsorption kinetics of monomeric TMPyP is much faster than those of  $ZnPcI_4$ , which is predominantly in dimeric form in aqueous solution (**Chapter 4.3**). The slow kinetics of the adsorption of  $ZnPcI_4$  can be rationally attributed to the slow monomerization and/or reorganization of the large molecules of  $ZnPcI_4$  on the surface of the nanofibers. The presence of NO-photodonor molecules slightly slows down both adsorption kinetics of TMPyP and  $ZnPcI_4$ .

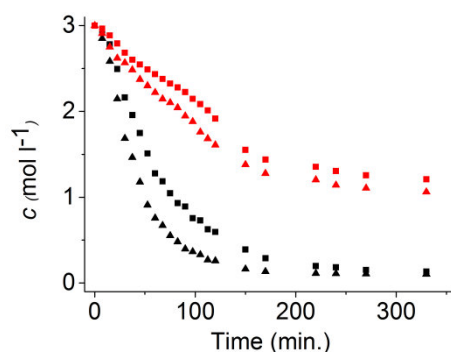


**Figure 4. 4.** Kinetics of adsorption of  $10^{-3}$ M TMPyP (black) or  $10^{-3}$ M ZnPcI<sub>4</sub> (red) in 20 ml of aqueous solution to 40 cm<sup>2</sup> of PS nanofiber material with (squares) and without (triangles) NO-photodonor. *c* designates concentration of the porphyrin/phthalocyanine in the loading solution after immersion of the nanofiber material.

An analysis of the adsorption kinetics after 6 hours of loading shows that material **N2** has 0.75 mmol g<sup>-1</sup> (0.68 mg TMPyP/1cm<sup>2</sup>) bonded TMPyP to the nanofiber material. Material **N3** is characterized by 0.46 mmol g<sup>-1</sup> (0.47 mg ZnPcI<sub>4</sub>/1cm<sup>2</sup>) bonded ZnPcI<sub>4</sub> molecules to the nanofiber material.

#### 4. 2. ATR-FTIR spectra

As shown in **Figure 4. 5.**, the original electrospun polystyrene exhibits main absorption bands at 1600, 1492 and 1451 cm<sup>-1</sup> (C=C aromatic stretching) and 1028 cm<sup>-1</sup> (C-H in-plane bending). Sulfonation of the polystyrene resulted in a strong band at 1036 cm<sup>-1</sup> and a doublet at 1210 and 1160 cm<sup>-1</sup>, which corresponds to the symmetric and asymmetric SO<sub>2</sub> stretching vibrations, respectively. The bands at 1127 and 1006 cm<sup>-1</sup> are assigned to the in-plane bending of the para-substituted phenyl ring, which confirms the successful sulfonation of the nanofiber.<sup>99</sup> Amination of the polystyrene is confirmed by the appearance of four characteristic bands: at 1326 cm<sup>-1</sup> (CF<sub>3</sub> stretching vibration), 1372 cm<sup>-1</sup> (NO<sub>2</sub> stretching vibration) and 1590 cm<sup>-1</sup> (N-H bending vibration) in the spectrum of **N1**. Moreover, the N-H bonds exhibit a wide intensive band around 3400 cm<sup>-1</sup> (not shown in **Figure 4. 5.**) that is also presented in the FTIR spectra of **N2** and **N3**. The narrow band from the deformation vibration of the N-methylpyridinium group at 1638 cm<sup>-1</sup> dominated the FTIR spectra of **N2** and it overlaps the band of N-H bending.<sup>100</sup> On the other hand, the binding of phthalocyanine is clearly confirmed in the spectrum of **N3** by the appearance of a band at 1502 cm<sup>-1</sup> which corresponds to the coupling of pyrrole and aza stretching. The adjacent band at 1489 cm<sup>-1</sup> is caused by an isoindole stretching vibration. The asymmetric stretching of the C-O-C bonds that connect methoxypyridinium groups to the phthalocyanine skeleton appear as a strong band at 1277 cm<sup>-1</sup>. The symmetrical stretching of this bond shows a small peak at 1048 cm<sup>-1</sup>, which is almost overlapped by the strong absorption of the -SO<sub>3</sub><sup>-</sup> group.<sup>101</sup>

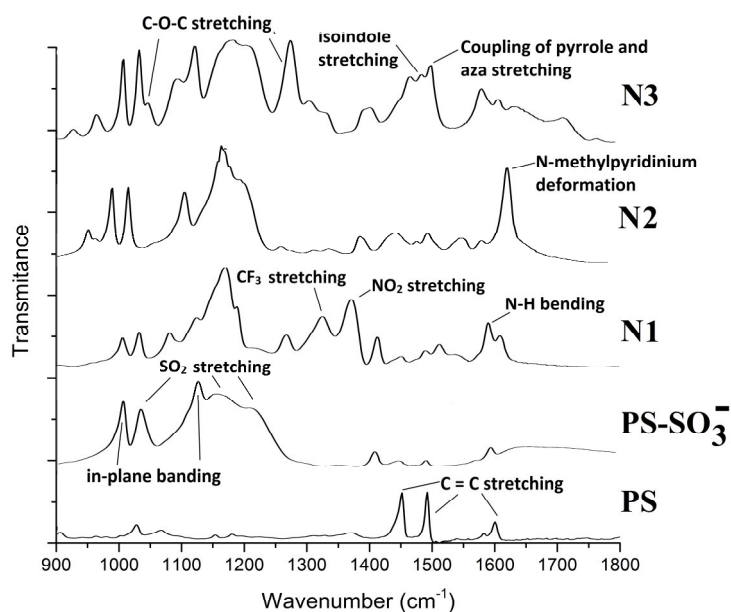


**Figure 4. 5.** FTIR of PS nanofiber material before (PS) and after surface derivatization by sulfonation (PS-SO<sub>2</sub>Cl), binding of NO-photodonor (N1) and next attachment of TMPyP (N2) or ZnPcI<sub>4</sub> (N3).

### 4. 3. UV/vis spectra

**Figure 4. 6.** shows the diffuse reflectance spectra of dry samples of prepared materials N1, N2, N3 and the corresponding absorption spectra of photoactive compounds in solutions. In the spectrum of N1 the absorption band of bound NO-photodonor at 387 nm is blue-shifted by 13 nm compared to the corresponding band of free NO-photodonor (at 400 nm) in aqueous solution. The blue shift can be attributed to the less polar character of nanofiber material with respect to water.<sup>59</sup>

The spectrum of N2 is characterized by the overlapping Soret bands for TMPyP (423 nm in aqueous solution) and NO-photodonor. Nevertheless the presence of characteristic Q-bands of TMPyP in the red region serves as an evidence for the surface modification by porphyrin.

Additionally, the spectrum of N3 exhibits a representative band for NO-photodonor that is partly overlapping with the Soret band of ZnPcI<sub>4</sub> in the blue spectral region. In the red region of the spectrum bands representative of the dimer and the prevailing monomer of ZnPcI<sub>4</sub> at 687 nm can be observed.<sup>97</sup> The bands are red-shifted by 10 nm with respect to its aqueous solution in which ZnPcI<sub>4</sub> exhibits absorption bands for its dimer at 630 nm and its monomer at 677 nm. The monomer form is predominant in less polar solvents (*e. g.* in dimethylformamide). **Figure 4. 6.** indicates that the dimerization of ZnPcI<sub>4</sub> found in aqueous solution, even at low concentration (10<sup>-6</sup>M), is considerably reduced after binding to the

nanofiber material. This fact is important as dimerization or higher aggregation generally significantly quenches the excited states and decreases the photoactivity of phthalocyanines.<sup>102</sup>

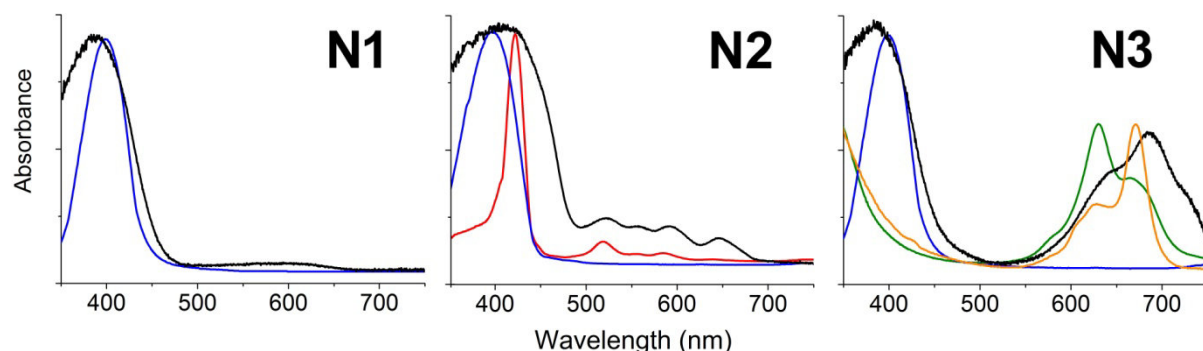


**Figure 4. 6.** Normalized diffuse reflectance spectra of dry samples (black lines) of **N1**, **N2**, **N3** and the absorption spectra of corresponding photoactive compounds in solutions. NO-photodonor (blue), TMPyP (red), ZnPcI<sub>4</sub> (green) in water and ZnPcI<sub>4</sub> (orange) in dimethylformamide.

#### 4. 4. O<sub>2</sub>(<sup>1</sup>Δ<sub>g</sub>) detection

The formation of O<sub>2</sub>(<sup>1</sup>Δ<sub>g</sub>) upon excitation of samples with TMPyP or ZnPcI<sub>4</sub> was confirmed by time-resolved phosphorescence at NIR. All measurements were performed in oxygen atmosphere with wet samples with humidity corresponding to saturated vapor pressure of D<sub>2</sub>O. The signals of O<sub>2</sub>(<sup>1</sup>Δ<sub>g</sub>) were averages of *ca.* 1000 traces and they were calculated as differences between signals in oxygen atmosphere and the detector responses in saturated vapor pressure of D<sub>2</sub>O. The initial part of the signals can fail due to strong prompt fluorescence of porphyrin/phthalocyanine and saturation of the detector and they were omitted in all figures.

The kinetics of both photosensitizer triplet states and oxygen O<sub>2</sub>(<sup>1</sup>Δ<sub>g</sub>) can be described using equation 4 and its simplified form for  $t \gg \tau_T$  (equation 5):

$$[O_2(^1\Delta_g)] = A_{SO} \frac{\tau_\Delta}{\tau_T - \tau_\Delta} (\exp(-t/\tau_T) - \exp(-t/\tau_\Delta)), \quad (4)$$

$$[O_2(^1\Delta_g)] = A_0 \exp(-t/\tau_\Delta), \quad \text{for } t \gg \tau_T, \quad (5)$$

where  $A_{SO}$  is a parameter,  $\tau_T$  is the lifetime of the photosensitizer triplet states in air atmosphere,  $\tau_\Delta$  is corresponding lifetime of O<sub>2</sub>(<sup>1</sup>Δ<sub>g</sub>),  $[O_2(^1\Delta_g)]$  denotes concentration of O<sub>2</sub>(<sup>1</sup>Δ<sub>g</sub>) in time  $t$  and  $A_0$  initial concentration of O<sub>2</sub>(<sup>1</sup>Δ<sub>g</sub>).

The results for excitation by an excimer laser (308 nm) are summarized in **Table 4. 1**.



**Table 4. 1.** Summary of the photophysical measurements. The lifetimes of the porphyrinoid triplet states ( $\tau_T$ ) and corresponding  $O_2(^1\Delta_g)$  lifetimes ( $\tau_\Delta$ ) of **N2** and **N3** in oxygen saturated  $D_2O$ .

System	Single exponential fit (eq. 5)	Double exponential fit (eq. 4)	
	$\tau_\Delta$ ( $\mu s$ )	$\tau_T$ ( $\mu s$ )	$\tau_\Delta$ ( $\mu s$ )
<b>N2</b>	29.9 $\pm$ 0.3	9.6 $\pm$ 0.2	30.7 $\pm$ 0.3
<b>N3</b>	25.9 $\pm$ 0.4	-	-

The **Figure 4. 7.** illustrates the signal of time-resolved near-infrared luminescence of  $O_2(^1\Delta_g)$  at 1270 nm of **N2** fitted by single exponential function.

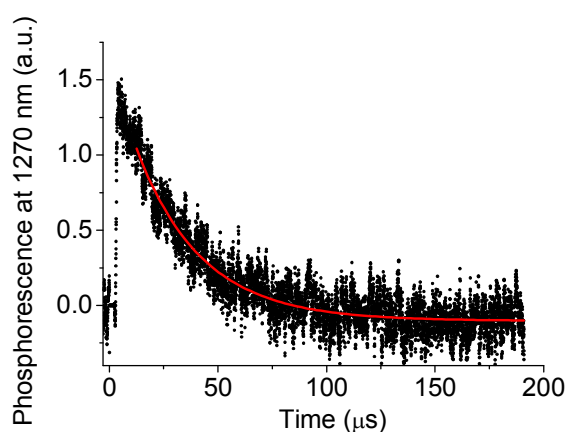


**Figure 4. 7.** Phosphorescence of  $O_2(^1\Delta_g)$  on the surface of **N2** (high TMPyP loading) calculated as difference between luminescence in oxygen saturated and in argon saturated  $D_2O$  after excitation of the sample by a 308 nm laser pulse at a high excitation energy ( $\sim 1.6$  mJ), average of 1000 traces.

The measured lifetime of  $O_2(^1\Delta_g)$  around 30  $\mu s$  for **N2** is significantly longer than in previously published data regarding nanofiber material with ionically attached TMPyP on the surface of sulfonated PS indicating suppressed quenching of  $O_2(^1\Delta_g)$  by surroundings. While the direct observation of time-resolved phosphorescence of  $O_2(^1\Delta_g)$  confirmed photogeneration of this species, the photoreleasing of  $O_2(^1\Delta_g)$  from the surface of **N2** and **N3** to aqueous solution was confirmed by two chemical methods, iodide detection<sup>34</sup> and photobleaching of uric acid.<sup>4</sup>

As an example, continuous irradiation of **N3** in aerated aqueous solutions of  $I^-$  was accompanied by a linear increase of the  $I_3^-$  concentration (proportional to photogeneration of  $O_2(^1\Delta_g)$ ) in the water phase (**Figure 4. 8. A**).



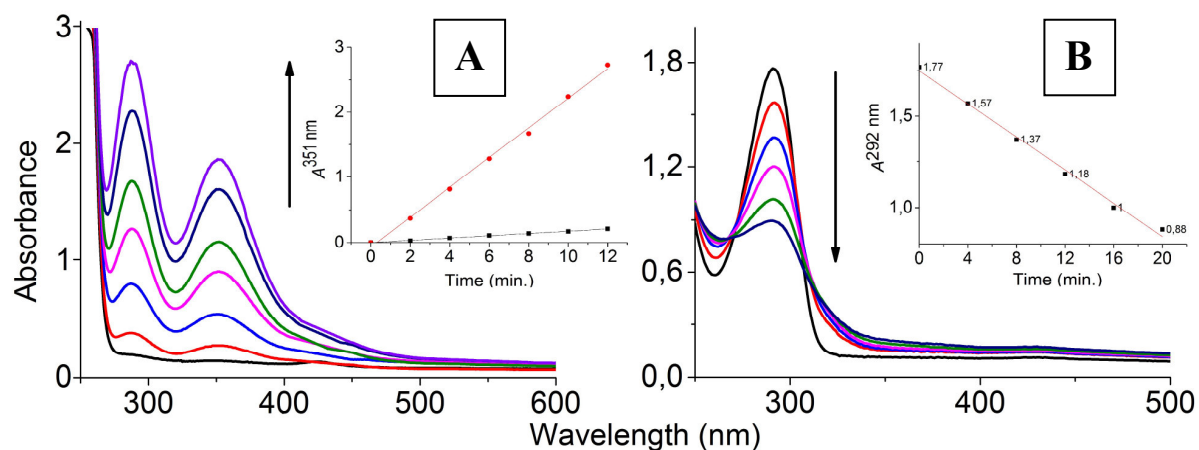


**Figure 4. 8. (A)** Absorption changes of 3ml air-saturated aqueous solution of 0.1M  $I^-$  containing TMPyP nanofiber materials ( $3 \text{ cm}^2$ ) during continuous irradiation by visible light ( $\lambda > 400 \text{ nm}$ ) at  $22^\circ\text{C}$ ; **Inset:** the time course of photogeneration of  $I_3^-$  (absorption band at 351 nm) in  $\text{H}_2\text{O}$  (red) and in the presence of 0.2M  $\text{NaN}_3$  (black). **(B)** Changes in absorption spectrum (**Inset:** absorption band at 292 nm) of 3 ml air-saturated  $2 \times 10^{-4} \text{ mol l}^{-1}$  uric acid in  $0.02 \text{ mol l}^{-1}$  phosphate buffer (pH = 7.0) containing  $3 \text{ cm}^2$  of **N2** during continuous irradiation (0-20 min) by visible light ( $\lambda > 400 \text{ nm}$ ) at  $22^\circ\text{C}$ , the arrow indicate the course of photooxidation.

The nanofiber materials in the dark and the irradiated photosensitizer-free materials did not produce any  $I_3^-$  because no  $\text{O}_2(^1\Delta_g)$  was generated. The formation of  $I_3^-$  was completely stopped in the presence of  $0.01 \text{ mol l}^{-1}$   $\text{NaN}_3$  (**Figure 4. 8. A, Inset**), which is an effective physical quencher of triplet states and  $\text{O}_2(^1\Delta_g)$ .<sup>34</sup>

The ability of **N2** and **N3** to photorelease  $\text{O}_2(^1\Delta_g)$  from the surface to aqueous solution was also verified using uric acid that is a known specific acceptor of  $\text{O}_2(^1\Delta_g)$ . The photobleaching reaction was monitored as the decrease of the uric acid absorbance peak at 292 nm (**Figure 4. 8. B**).

No release of any photoactive compounds from the nanofiber surfaces to the water phase was detected.

#### 4. 5. NO detection

All prepared materials (**N1**, **N2**, **N3**) exhibit NO being released from the surface when irradiated by visible light. **Figure 4. 9. A** illustrates the release of NO from all materials immersed in  $\text{H}_2\text{O}$  detected by the amperometric method.<sup>81</sup> Amperometric NO detection allows for the quantification of generated gas. The switch-on/switch-off cycling of the excitation laser demonstrates a stable and controllable NO release as well as the trigger character of the light (**Figure 4. 9. B**). The process of amperometric detection is accompanied with a delay in electrode response which can be attributed to a time necessary for diffusion of photoreleased NO from the nanofiber surface to the electrode.

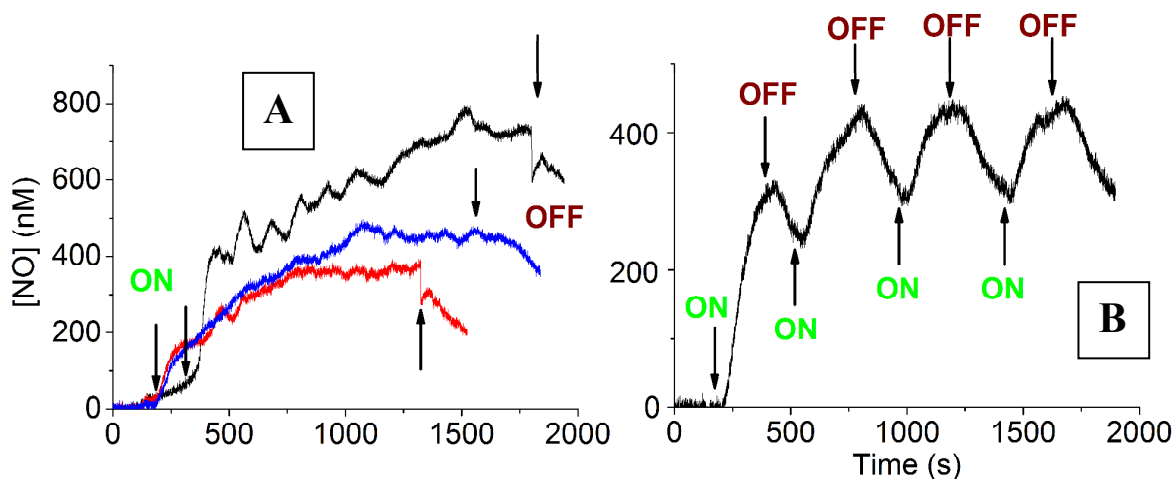


**Figure 4. 9.** (A) The amperometric detection of NO photoreleasing from the surface of N1 (black), N2 (red) and N3 (blue) placed on quartz plate in plastic cuvette with H<sub>2</sub>O by amperometric method. H<sub>2</sub>O without the sample was used as a negative control. The arrows indicate switch-on and switch-off character of NO releasing triggered by the irradiation (100 mW laser, 405 nm). (B) The cycling of switch-on and switch-off of the excitation 100 mW laser (405 nm, illustrated on N1).

Besides the use of amperometric detection, other simple chemical methods were employed in order to establish the propensity of the new materials to photorelease NO.

DAN assay represents one of the most sensitive and selective fluorescence-based methods for NO detection. As is evident from **Figures 4. 9. A** and **4. 10. A**, under strictly the same experimental conditions (for details see **Chapter 3. 9.**), the greatest amount of photoreleased NO was observed for N1. The lower amount of NO photoreleased from the surface of N3 and especially N2 (**Figure 4. 10. A**) can be attributed to the filter effect of the bound porphyrinoids. The Soret band of TMPyP in N2 overlaps with the absorption band of NOP, which leads to a lower quantity of released NO. The smaller overlap of the absorption bands of ZnPcI<sub>4</sub> with NOP in blue region causes a decrease of NO production as well, albeit a significantly lower one.

The photoreleased NO from the surfaces of N1, N2 and N3 materials was also followed by myoglobine test. Equine skeletal myoglobin (Mb) similarly to other haem proteins, binds NO through its metal center.<sup>103</sup> The binding of NO photoreleased from nanofiber materials to Mb was observed in absorption spectra of Mb (**Figure 4. 10. B**). The appearance of a Soret band at 420 nm confirms binding NO to the Fe(II) of the haem group of Mb.<sup>104</sup> Control experiments performed that irradiated solutions containing reduced Mb in the absence of N1, N2, N3 or in the presence of NO-photodonor-free nanofiber materials, did not result in the formation of the adduct.

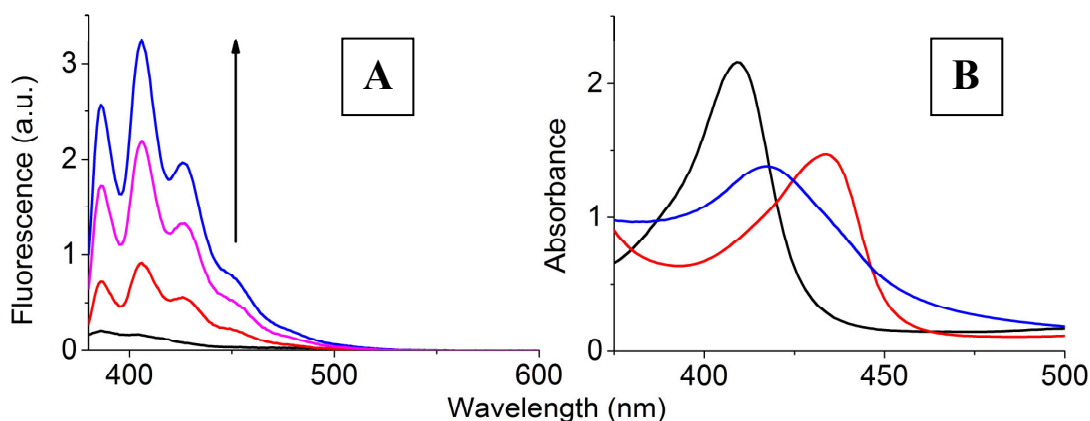


**Figure 4. 10. (A)** The fluorescence detection of NO photoreleasing from the surface of **N1** (blue), **N2** (purple), **N3** (red) by DAN method. The fluorescence ( $\lambda_{exc} = 365$  nm) of the 3.5 ml of 0.31 mM DAN in 0.62 M HCl with of nanofiber material ( $8 \text{ cm}^2$ ) before (black) and after 50 min of irradiation (indicated by arrow) by 500W xenon lamp with long pass filter ( $\lambda \geq 400$  nm). **(B)** The myoglobin test for detection of NO releasing from the surface of **N2** after 2 min of irradiation by 400W Xe lamp with long-pass filter ( $\lambda > 400$  nm) at  $22^\circ\text{C}$ . 3 mM Mb(Fe<sup>III</sup>) in 0.02 M phosphate buffer, pH = 7.0 (black), its reduced form Mb(Fe<sup>II</sup>) before (red) and after binding of released NO (blue).

#### 4. 6. Antibacterial activity

The antibacterial properties of the nanofiber materials with ionically attached or encapsulated photosensitizers and their strong bacteria inhibition on their surface (**Figure 1. 3.**) have been already extensively studied in our laboratory.<sup>29,38-42</sup> Nevertheless, NO generated from the surface of nanofiber materials with longer lifetime ( $\approx 3$  s) and consequently longer diffusion pathway can cause sterilization of a large area in comparison to nanomaterials photogenerating just  $\text{O}_2(^1\Delta_g)$  with short lifetime and diffusion pathway.

In order to confirm this, the following antibacterial experiment was performed: The nanofiber materials **N1**, **N2** and **N3** were immersed in suspensions of *E. coli* and irradiated with a daylight simulator or kept in the dark (for experimental details see **Chapter 3. 12.**).

**Figure 4. 11.** illustrates very strong, almost total bacterial growth inhibition of *E. coli* after 10 min of irradiation of a 1 ml bacterial suspension in the presence of **N1**. Similar observations were found for **N2** and **N3** materials.

Nanofiber materials without NOP or materials with NOP kept in the dark did not exhibit any bacterial inhibition compared to the control (irradiated/dark bacterial suspension without any nanofiber material). Also nanofiber materials with ionically attached photosensitizers (TMPyP or ZnPcI<sub>4</sub>) did not exhibit noticeable bacterial inhibition in suspension due to the short lifetime and pathway of  $\text{O}_2(^1\Delta_g)$ , which enables just the sterilization of nanofiber material surfaces.

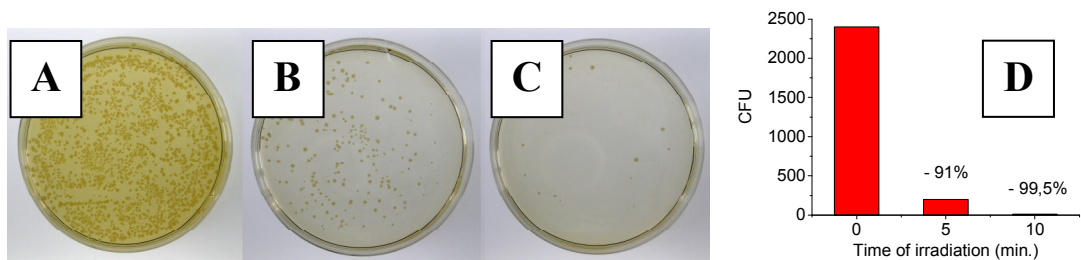


**Figure 4. 11.** Antibacterial activity of N1 in suspension of *E. coli* without irradiation ( $\lambda > 400$  nm) (A), after 5 minutes irradiation (B), or 10 minutes irradiation (C) with 400W solar simulator. (D) The corresponding graph with the number colonies formation units. Experimental conditions – see **Chapter 3. 12.**

Evidently, the nanofiber materials containing NOP increase the antibacterial range and possible usefulness of nanofiber materials doped by photosensitizers for medical application. On the other hand, one important disadvantage remains: the amount of released NO is limited by the quantity of NOP in materials. One molecule of NOP can release only one molecule of NO which differs from the photosensitizer that can repeatedly generate  $O_2(^1\Delta_g)$  (depends on photosensitizer photostability).

The investigation of the ideal NOP/photosensitizer ratio and its influence on surface, space and time dependent antibacterial activity was beyond the scope of this thesis.

## 5. Results and discussion for Aim II

### 5. 1. Reversible binding of NO onto dimetallaborane [*closo*-(PMe<sub>2</sub>Ph)<sub>4</sub>Pt<sub>2</sub>B<sub>10</sub>H<sub>10</sub>]

As have been shown and described previously, NO-photodonors are irretrievably chemically changed after NO generation. A system that is able to repeatedly bind and release NO is therefore highly desirable. One possible system that might meet this requirement is based on boron containing clusters and was investigated for this purpose during this work (for details see **Chapter 1. 8. 2.**).

Since the discovery that the dimetallaborane [*closo*-(PMe<sub>2</sub>Ph)<sub>4</sub>Pt<sub>2</sub>B<sub>10</sub>H<sub>10</sub>] (**B1**) reversibly sequesters atmospheric oxygen, the system has been shown to also bind the gases CO and SO<sub>2</sub>.<sup>65</sup> In a logical progression to this work, relevant to the scope of this thesis, we set to investigate the propensity of **B1** to capture nitric oxide (NO), a gas with similar anti-bacterial properties as singlet-oxygen but with the advantage of a considerably longer lifetime.

Thus, **B1** was prepared and purified for NO capture investigation using the published procedure.<sup>65</sup>

Photogeneration of NO from nanofiber material **N1** was used as a source of nitric oxide using 200 mW diode laser for the excitation (iBeam Smart,  $\lambda = 402$  nm). Several experiments aimed at the photogeneration of NO from **N1**, followed by condensation of the gas into a recepticle tube containing **B1**, as shown in **Figure 5. 1.**, and subsequent capture on **B1** were tried.

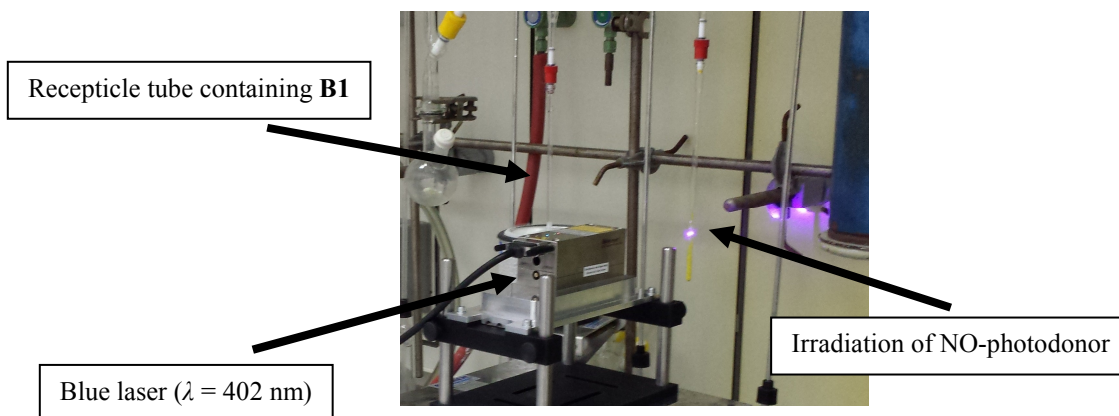


**Figure 5. 1.** Scheme of NO capture experiment using 200 mW diode laser ( $\lambda = 402$  nm) for NO generation.

However, the concentrations of NO gas released by this method (measured in the hundreds of nanomoles over a period tens of minutes (**Chapter 4. 5.**) were too low and thus unsuitable for this purpose. In most of the experiments, a standard chemical method using the action of dilute nitric acid on sodium nitrite under an inert atmosphere of argon was employed for convenient generation of NO in larger amount:

In a typical experiment, 0.244 g (3.5 mmol) of  $\text{NaNO}_2$  was dissolved in 10 ml of deaerated distilled water and stirred under an inert atmosphere of argon in three-necked round-bottomed flask. Then 5 ml of 15 mmol  $\text{HNO}_3$  (also in deaerated distilled water) was added *via* addition funnel. Into a different three-necked round-bottomed flask containing magnetic stir bar and 30 mg (35  $\mu\text{M}$ ) of **B1**, *ca.* 10 ml of dichloromethane was condensed. NO was delivered *via* closeable connection with needle (**Figure 5. 2.**).

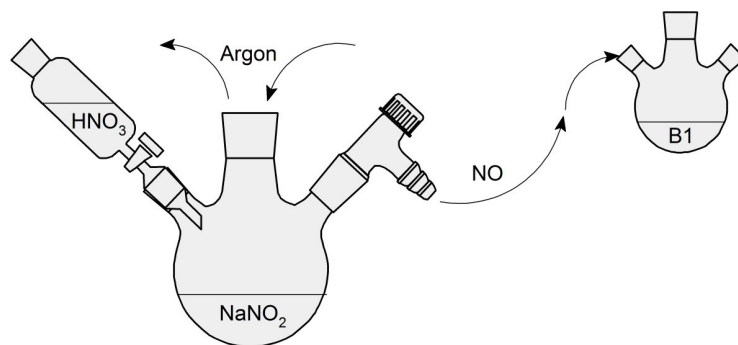


**Figure 5. 2.** The simplified diagram of the apparatus for NO preparation.

After only short mixing times (couple of seconds) of NO with **B1**, a clear colour change from purple to yellow was observable to the eye and monitored using UV/vis spectroscopy, which parallels previously obtained data for the reaction of **B1** with  $\text{O}_2$ ,  $\text{SO}_2$  and  $\text{CO}$  gases. As may be seen in **Figure 5. 3.**, the main absorption peak for **B1** at 521 nm disappears after the binding of NO on the metal-metal two atom vector.

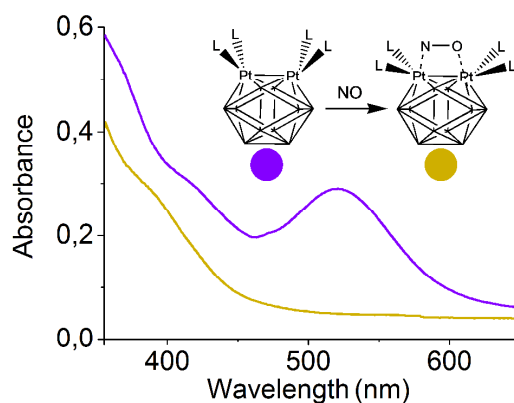


**Figure 5. 3.** UV/vis spectrum of **B1** (purple) and **B1-NO** (yellow). with suggested capture of NO gas by **B1**.

Passage of NO through a solution of **B1** yields **B1-NO** quantitatively as determined by  $^{11}\text{B}$  NMR spectroscopy. A summary of the chemical shifts of all relevant species may be seen in **Table 5. 1**. Saturation of a dichloromethane solution of **B1** with NO led to the disappearance of the signature  $^{11}\text{B}$  NMR chemical shift peaks associated with (**B1**) and the emergence of new peaks indicated in the same **Table 5. 1**. as **B1-NO**. The assignment of the chemical shift peaks were made on the basis of relative intensities and cross-over peaks in  $^{11}\text{B}$ - $^{11}\text{B}$  CO-SY NMR experiments. In summary, four peaks with an intensity ratio 2:2:2:4, expected for

the molecular symmetry of **B1**-NO are observed. Of particular note is the *ca.* 40 ppm downfield shift for the B(8,10) peak, indicating a large deshielding effect of NO molecular capture. This significant increase in deshielding after the gas binding across Pt-Pt vector can also be observed for the B(3,6) signal. In this regard, it is a similar deshielding pattern to that of **B1**-O<sub>2</sub>, which might suggest a linear rather than perpendicular attachment of the NO molecule across the Pt-Pt vector (**Figure 5. 3.**).

**Table 5. 1.** <sup>11</sup>B NMR data for **B1** and corresponding gas adducts.\*

Compound	$\delta(^{11}\text{B})/\text{ppm}$			
	B(3,6)	B(9,12)	B(8,10)	B(4,5,7,11)
<b>B1</b> -NO	25.7	17.3	10.2	3.6
<b>B1</b> -SO <sub>2</sub>	11.5	21.4	-9.7	4.5
<b>B1</b> -CO	5.9	14.0	-15.3	2.6
<b>B1</b> -O <sub>2</sub>	18.6	16.1	-2.4	2.1
<b>B1</b>	16.9	22.0	-31.1	25.4

\* note that 10-vertex *nido*-B<sub>10</sub>H<sub>14</sub> and 11-vertex *nido*-type clusters have a numbering convention different from that of the 12-vertex *nido*-type clusters of the other compounds

Conversely, higher shielding is experienced by the boron atoms B(4,5,7,11) which follows the pattern in the <sup>11</sup>B spectra of other **B1**-gas adducts.

The purging of NO adduct solutions with inert gases (dinitrogen, argon), or evaporation of solvent under reduced pressure, does not remove NO to regenerate **B1**, as is the case for O<sub>2</sub>. It is reasonable that UV irradiation (as is the case for CO and SO<sub>2</sub>) will be required for gas removal. A deeper investigation of reversibility of NO binding on **B1** using UV irradiation, and a crystal structure analysis of **B1**-NO were beyond the scope of this thesis, but it remains a part of our continuing research.



Nevertheless, we have opened the possibility that our system could be an interesting alternative to current organic-based NO-photodonors that are irretrievably chemically changed after NO release. Moreover, our system could be employed for high-density NO storage and real-time NO concentration sensing.

## 5. 2. Preparation of new monometallaborane species

A key aspect for the development of small-molecule capture on bimetallic borane frameworks is the ready availability of monometallaborane species with various ligand and metal systems. Concordantly, an aim of this thesis is the syntheses of such new monometallaborane species.

The starting borane material for the purposes of the new metallaborane syntheses was *nido*-decaborane - a compound that is relatively cheap and commercially available. Its  $^{11}\text{B}$  NMR spectrum shows expected shifts and intensities that are consistent with its 2:2:4:2 molecular symmetry (**Figure 5. 4.**)

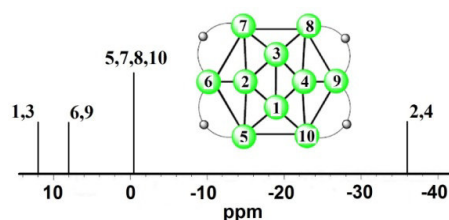


**Figure 5. 4.**  $^{11}\text{B}$  NMR spectrum of the starting material, *nido*- $\text{B}_{10}\text{H}_{14}$ .

The *nido*- $\text{B}_{10}\text{H}_{14}$  cluster possesses an open face with four divalent bridging hydrogen atoms that are acidic in character and can be cleaved using appropriate bases. The deprotonated *nido*-decaboranyl anion is an excellent Lewis base, and therefore subsequent addition of metallaphosphines with general formula  $(\text{PR}_3)_2\text{MCl}_2$  result in the formation of monometallaborane species (**Figure 5. 5.**), generally in high yields of around 70% (**Table 5. 2.**), without substantially perturbing the essence of the *nido*-decaboranyl bonding system, *i. e.* two B-H-B bridging bonds are replaced with two B-M-B bonds.

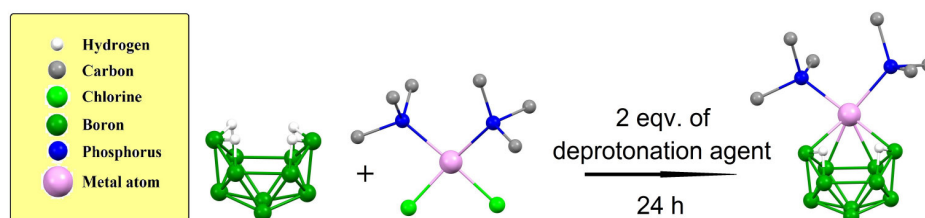


**Figure 5. 5.** General scheme of the monometallaborane syntheses (hydrogen atoms, except the bridging hydrogen atoms in the borane cluster, were removed for clarity).



In a typical experiment was used bdmn as a deprotonation agent due to its stability and easy handling. The synthesis of **M5** using the bdmn deprotonation agent led to the ionic *bis*-decaboranyl  $[B_{10}H_{12}\text{-Pt-B}_{10}H_{12}]^{2-}[\text{bdmnH}]_2^+$  sandwich complex. This particular reaction pathway is more common for Pd or Ni complexes and rarely occurs with Pt. Using methylated metal complexes of type  $[ML_n(\text{Me})_2]$  avoids the necessity of a base to remove two bridging hydrogen atoms from the borane cluster and yields are almost quantitative (>90%) - The only side product of the reaction being methane gas. Otherwise, the rest of the synthetic procedure remained identical. Using bdmn for the synthesis of **M7** generates a wide spectrum of unstable side products, but with the stronger base ( $\text{KHBET}_3$ ) and shorter reaction time ( $\approx 2$  hours) the desired monometallaborane can be obtained in a reasonable yield, which is still only half the yields of the other monometallaborane compounds described here (**Table 5. 2.**).

**Table 5. 2.** Summary of new monometallaboranes syntheses.

Compound	Crystals colour	Yield	Compound	Crystals colour	Yield
<b>M1</b>	yellow	80%	<b>M5</b>	yellow	92%
<b>M2</b>	yellow	78%	<b>M6</b>	orange brown	75%
<b>M3</b>	dark orange	80%	<b>M7</b>	orange brown	45%
<b>M4</b>	yellow	64%			

Due the good solubility of monometallic species in dichloromethane and efficient movement on silica, it follows that they can be relatively easily purified with high yields using flash chromatography performed on silica as the fastest eluting band. Conversely, the *bis*-decaboranyl metal complexes are poorly soluble in dichloromethane, which can serve as a first evidence of their formation because  $^{11}\text{B}$  NMR spectrum is generally very similar to the monometallaboranes. The crystal structures are depicted on **Figure 5. 6.**

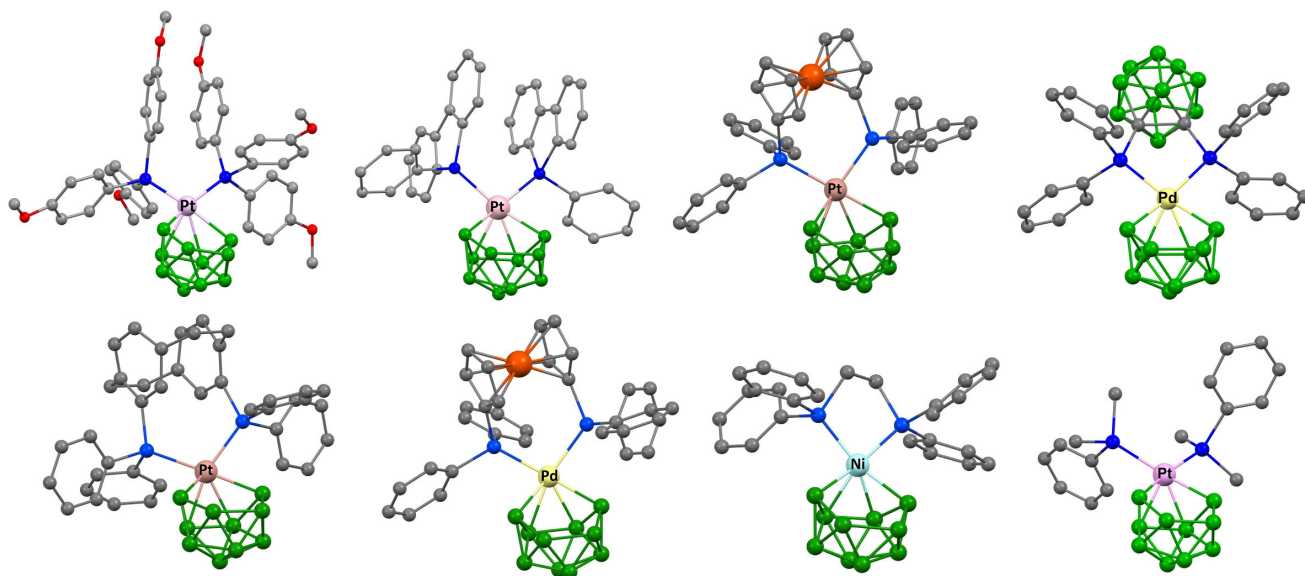


**Figure 5. 6.** The molecular structures of (from top left) **M1**, **M2**, **M3**, **M4**, **M5**, **M6**, **M7** and **Mk** as determined by single-crystal X-ray diffraction analysis (hydrogen atom have been removed for clarity).

### 5. 2. 1. NMR data

The  $^{11}\text{B}$  NMR spectra of **M1-3** and **M6-7** are consistent with the expected monometallaborane cluster geometry - six signals with 1:1:2:2:2:2 intensity patterns. The resulting spectra are comparable to the known metallaborane cluster  $(\text{PMe}_2\text{Ph})_2\text{PtB}_{10}\text{H}_{12}$  (**Mk**).<sup>73</sup>

The boron atoms 2, 3, 8 and 11 are directly connected to the metal center and thus are most affected by the metal and ligand changes. Larger ligands (compared to  $\text{PMe}_2\text{Ph}$  in **Mk**) on metal atoms causes generally higher deshielding, thus the chemical shifts for B(2,3) and B(8,11) signals move to the left end of the spectrum. These shifts result in overlapping of the B(5) atom peak which is difficult to observe especially in the **M1** and **M2**  $^{11}\text{B}$  NMR spectra (the data are summarized in the **Table 5. 3**).

**Table 5. 3.**  $^{11}\text{B}$  NMR data for monometallaboranes in  $\text{CDCl}_3$  solution at 298–300 K with the structure and numbering of monometallaborane cluster.\*

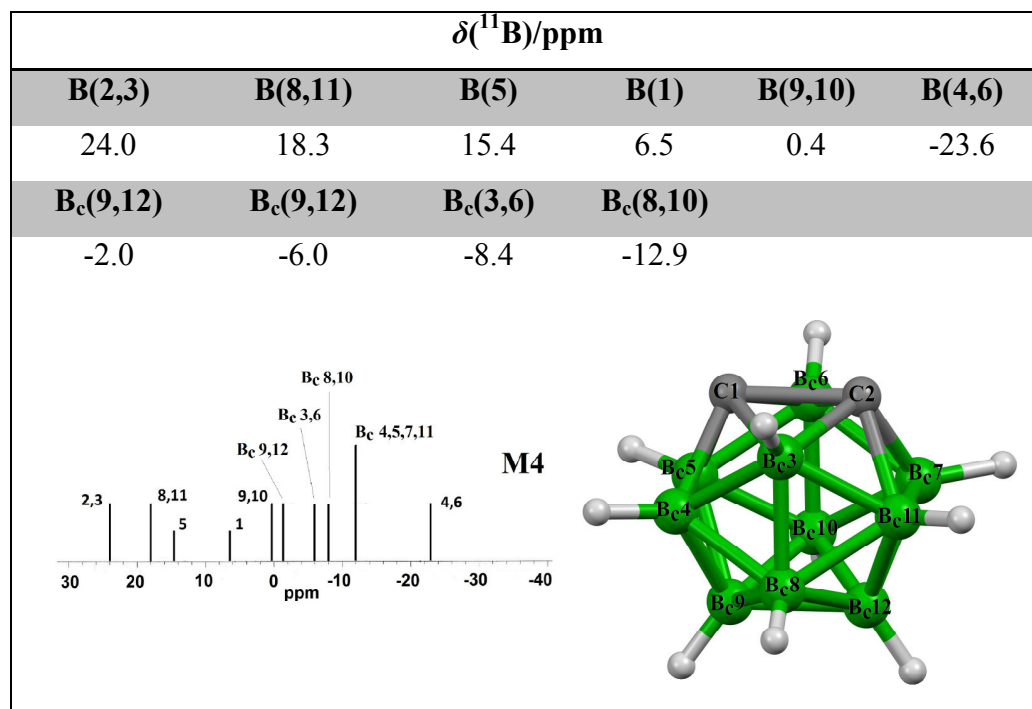
Compound	$\delta(^{11}\text{B})/\text{ppm}$					
	B(5)	B(2,3)	B(8,11)	B(1)	B(9,10)	B(4,6)
M1	11.9	17.7	14.5	2.3	-3.0	-24.7
M2	10.7	16.3	9.9	1.8	-3.5	-26.2
M3	9.1	12.9	8.0	-2.1	-7.4	-29.3
M6	14.5	19.8	16.3	2.3	-3.0	-26.5
M7	12.4	16.1	10.9	4.9	-2.1	-22.1
Mk	11.3	10.2	4.8	-2.1	-7.5	-31.3

\* note that 10-vertex *nido*- $\text{B}_{10}\text{H}_{14}$  and 11-vertex *nido*-type clusters have a numbering convention different from that of the 12-vertex *nido*-type clusters of the other compounds

The interpretation of  $^{11}\text{B}$  NMR spectrum of **M4** (**Table 5. 4.**) is more complex due the presence of the carborane cluster ligand, which exhibits four signals with an intensity pattern of 2:2:2:4 consistent with its molecular symmetry. The assignment of the  $^{11}\text{B}$  chemical shift peaks were made on the basis of their relative intensities and symmetry considerations, as well as cross-over peaks in  $^{11}\text{B}$ - $^{11}\text{B}$  COSY NMR experiments that show direct connectivities between individual peaks.

**Table 5. 4.**  $^{11}\text{B}$  NMR data for **M4** in  $\text{CDCl}_3$  solution at 298–300 K with the structure and numbering of carborane cluster.



For the purposes of further investigation into the molecular dynamics of the new monometallicdeca-boranyl compounds,  $^{31}\text{P}$  NMR spectra were recorded (**Table 5. 5.**). In the case of the platinum containing compounds (**M1-3**), the only observable couplings with  $^{31}\text{P}$  nuclei were those with  $^{195}\text{Pt}$  nuclei (spin quantum number  $I = 1/2$  and 33.7 natural abundance), which result in so-called „platinum satellites“: separation of the signal into a doublet or satellite lines. Other compounds exhibit expected singlet peak in the spectrum.

**Table 5. 5.**  $^{31}\text{P}$  NMR data for monometallaboranes in  $\text{CDCl}_3$  solution at 298–300 K.

Compound	$\delta(^{31}\text{P})/\text{ppm}$			$J(^{195}\text{Pt}-^{31}\text{P})/\text{Hz}$
<b>M1</b>	32.9	25.1	17.3	1278
<b>M2</b>	28	20.5	13	1222
<b>M3</b>	39.7	31.6	23.5	1314
<b>M4</b>	69.2			
<b>M6</b>	23.8			
<b>M7</b>	54.1			

Of particular noteworthiness is the product **M5**: All other new 11-vertex metallaborane species reported in this thesis are molecules with precise mirror-plane symmetry in solution phase. Only **M5** differs from this sequence: Its  $^{11}\text{B}$ ,  $^1\text{H}$  and  $^{31}\text{P}$  NMR spectra all suggesting

asymmetry (**Table 5. 6.**) in the solution phase - 10 resonance peaks in the  $^{11}\text{B}-\{^1\text{H}\}$  spectrum, and two peaks in the  $^{31}\text{P}-\{^1\text{H}\}$  spectrum with related sets of „platinum satellites“.

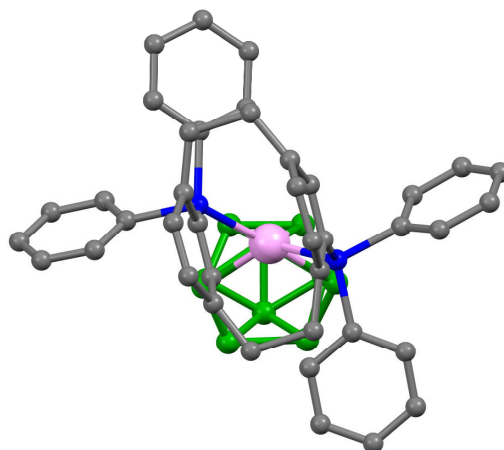
**Table 5. 6.**  $^{11}\text{B}$  and  $^{31}\text{P}$  NMR data for **M5** in  $\text{CDCl}_3$  solution at 298–300 K.

$\delta(^{11}\text{B})/\text{ppm}$									
B(2)	B(3)	B(8)	B(11)	B(5)	B(9)	B(10)	B(1)	B(4)	B(6)
20.0	17.8	14.8	12.1	7.8	1.1	-2.3	-5.5	-26.0	-28.1

$\delta(^{31}\text{P})/\text{ppm}$			$J(^{195}\text{Pt}-^{31}\text{P})/\text{Hz}$
54.6/53.8	46.4/45.6	38.2/37.4	1311

This asymmetry is also seen in the solid-state structure as determined by single-crystal X-ray diffraction studies, which reveals an asymmetric conformation of the (S)-(+)-4,12-bis(diphenylphosphino)-[2.2]-(paracyclophane) ligand (commonly referred to as (S)-phanephos) around the platinum(II) centre in relation to the borane cluster (**Figure 5. 7.**).



**Figure 5. 7.** Aerial perspective of the molecular structure of **M5** (hydrogen atoms have been omitted for clarity).

**M5** was formed on the reaction of *nido*- $\text{B}_{10}\text{H}_{14}$  with ligand **MP5** in the presence of base. The precursor to the  $C_2$ -symmetric planar chiral diphosphine ligand **MP5** is available as two enantiomers – (R)-(-)- and (S)-(+)- 4,12-bis(diphenylphosphino)-[2.2]-paracyclophane, commonly referred to as (R)- and (S)-phanephos (**Figure 5. 8.**). The chiral environment is generated by the ancillary groups on the phosphines, with [2.2]paracyclophane acting as a scaffold.<sup>92</sup>

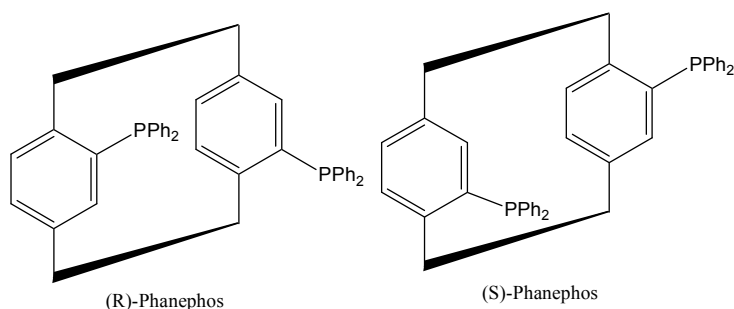


**Figure 5. 8.** Schematic representation of the two enantiomers of phanephos.

For the synthesis of **MP5**, only one enantiomer, (S)-Phanephos was used, and resulted in the clean formation of (S)-(+)-4,12-Bis(diphenylphosphino)-[2.2]-(paracyclophane) dimethylplatinum(II) as shown in **Table 3. 1.**  $^{31}\text{P}$  NMR spectroscopy clearly supports this assessment. Therefore, we can exclude the possibility of a misinterpretation of the NMR data as a mixture of equal quantities of two similar isomers. The interesting question here, is why does the (S)-phanephos ligand in **M5** seem to favour an asymmetric alignment? It occurred to us that this particular conformation may be temperature sensitive, and that at higher thermal energies the (S)-phanephos ligand could flip to other positions. Therefore, we carried out variable temperature  $^{11}\text{B}$  and  $^{31}\text{P}$  NMR experiments at increments of 10 °C up to a temperature of 70 °C (we were limited to this temperature by the nature of suitable available NMR solvents). At these temperatures no change was observed in the NMR spectra, indicating at least a good stability, if not permanence, of this particular conformation (we hope to investigate by NMR at yet higher temperatures in due course). An asymmetric conformation of the [1,1'-bis(diphenylphosphino)ferrocene] ligand is also seen in the crystal structures of **M3** and **M6**, however, solutions of these compounds have symmetrical NMR spectra (**Table 5. 3.**) suggesting a 'hopping' or 'flipping' movement of the phosphino ligands such that in solution an average is observed. It is conceivable that the  $\{\text{C}_2\text{H}_4\}$  groups connecting the two aromatic rings in the phanephos ligand prevent such a flexibility in the case of **M5**, preserving the solid-state asymmetry in solution phase.

### 5. 2. 2. General considerations on bond connectivity lengths and bond angle in compounds M1-M7

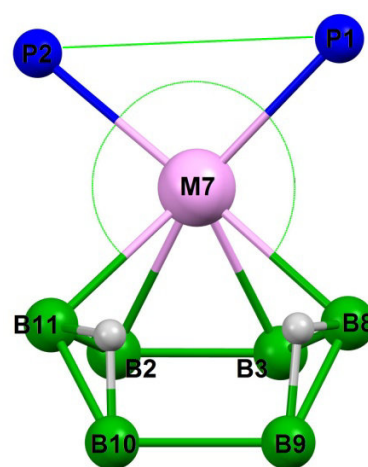
The lengths of B-B connectivities in the boron clusters of the new metallaborane species M1-M7 have generally standard lengths of around  $\approx 1.78$  Å with exception of the connectivities between boron atoms on the cluster open-face, where lengthening is observed. B(2)-B(3) bonds are widened generally to 1.86 Å, even greater lengthening is observed for B(9)-B(10) bond: 1.95 Å (longest for **M7** - 1.99 Å). Bonds B(8)-B(9) and B(10)-B(11) also exhibit small lengthening of 0.3-0.4 Å. For details see **Table 5. 7**.

**Table 5. 7.** Atom distances and angles in new monometallaborane crystal structures.

Compound	P-M-P (°)	B(8)-M-B(11)	P(1)-M-B(8)	P(2)-M-B(11)
<b>M1</b>	95	92	97	79
<b>M2</b>	94	89	82	90
<b>M3</b>	97	90	84	87
<b>M4</b>	92	92	86	86
<b>M5</b>	102	91	81	86
<b>M6</b>	97	90	84	87
<b>M7</b>	87	97	85	86
<b>Mk</b>	97	94	89	78

Compound	P-P (Å)	P(1)-M	P(2)-M	B(8)-M	B(11)-M	B(2)-M	B(3)-M
<b>M1</b>	3.53	2.32	2.46	2.42	2.09	2.32	2.52
<b>M2</b>	3.40	2.34	2.34	2.30	2.34	2.23	2.25
<b>M3</b>	3.52	2.36	2.34	2.32	2.30	2.25	2.24
<b>M4</b>	3.32	2.31	2.32	2.31	2.30	2.25	2.25
<b>M5</b>	3.72	2.40	2.39	2.33	2.29	2.24	2.25
<b>M6</b>	3.56	2.40	2.36	2.32	2.31	2.25	2.26
<b>M7</b>	3.03	2.21	2.19	2.22	2.20	2.14	2.12
<b>Mk</b>	3.49	2.34	2.33	2.31	2.36	2.22	2.20



The distances between the two phosphorus atoms are dependent on the ligands size, hence the **M5** has the greatest distance (3.72 Å), thus the largest P-M-P angle (107°). On the other hand, the shortest distance (3.03 Å) and smallest angle (87°) are in **M7** molecule which agrees with expectations. The remainder of the monometallic compounds have average P-P distances of about 3.45 Å with P-M-P angles *ca.* 95°.

The monodentate ligands exhibits freer movement of their functional groups, thus bigger distinction between P(1)-M-B(8) and P(2)-M-B(11) angles (>12°, even 18° for **M1**) and are more comparable to the known monometallic precursor (11°). Due the bidentate character of ligands in **M3-M6**, and hence the movement restrictions of phosphine ligands, the differences here are generally below 6°.

The lengths of B-B connectivities in the carborane cluster from **M4** also have generally standard lengths of around  $\approx$  1.78 Å. The lengths of C-B connectivities are shorter  $\approx$  1.71 Å which agrees with expectations.

### 5. 2. 3. The choice of ligand in the syntheses of new 11-vertex metallaborane compounds

All seven new monometallic compounds, **M1-M7**, were used as precursors for the syntheses of their respective bimetalaborane cluster systems by the deprotonation of the remaining two cluster bridging hydrogen atoms followed by insertion of a second {Metal-Ligand} fragment. This is a complicated and difficult synthetic step, requiring very rigorous anaerobic conditions, and as yet our attempts have so far proved unsuccessful probably due to steric hinderance of the new ligands to the insertion of the second {ML<sub>2</sub>} fragment compared to that of PMe<sub>2</sub>Ph. However, some NMR evidence for bimetallic species formation were obtained under certain conditions for several of the new monometallic compounds, but the stability of these products were very poor, and no pure or crystalline samples were isolated. Nevertheless, work continues on this aspect.

The choice of what ligand systems to use in the syntheses of **M1-M7** was made for the following reasons: **M3** and **M6** may well have interesting electrochemical properties due to the presence of two metals which are planned to be studied soon. **M1** offers the possibility for further chemical modification via its -OCH<sub>3</sub> groups. As an example can serve the catalyzed functionalization of anisole with fullerene by homolytic C-H bond cleavage (**Figure 5. 9**).<sup>105</sup> This is of particular interest to us as fullerene moieties can function as light-harvesting „antennas“ that could possibly pass on energy towards the small molecules captured on the metal centres of the bimetallic system.



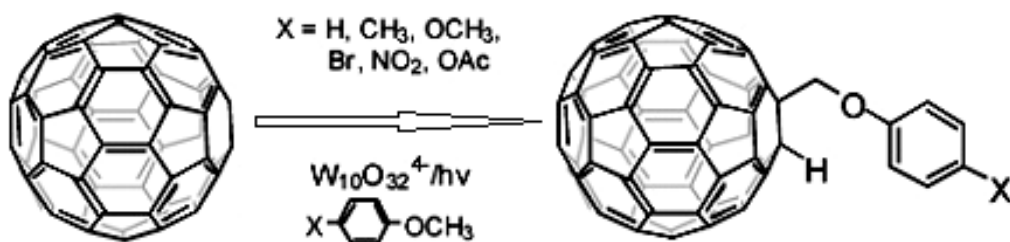


**Figure 5. 9.** Reaction scheme of catalyzed functionalization of anisole.<sup>105</sup>

**M2-7** were also synthesized in order to investigate their photophysical properties as potential light-harvesting antennae. It was hoped that the sterically constrained aromatic systems in **M2**, **M5** and **M7** in particular would lead to interesting absorption and emission of light. However, no fluorescence or other emission have yet been detected. Moreover, **M5** could possess catalytic properties - Chiral bisphosphines such as (4,12-bis(diphenylphosphino)-[2.2]-paracyclophane and their derivatives have proved to be among the most useful and versatile ligands in the area of organotransition metal-catalyzed reactions, namely asymmetric hydrogenation.

## 6. Conclusion

The work in this thesis has shown that electrospun polystyrene nanofiber materials chlorosulfonated with chlorosulfonic acid are good and appropriate substrates for the subsequent modification with photoactive molecules (photosensitizers and NO-photodonor) that can effectively generate singlet oxygen and nitric oxide on exposure to daylight. These photofunctional nanofiber materials simultaneously photogenerate small antibacterial species NO and  $O_2(^1\Delta_g)$ . The photogeneration of these species were verified amperometrically, using time resolved spectroscopy and by chemical detection methods. The strong antibacterial effect was demonstrated on *E. coli*. The new nanomaterials offer several functionalities that are important in the development of medical materials (*e. g.* for covering of chronic wounds): **i)** the ability to detain bacteria and other pathogens on its nanoporous surface **ii)** the sterile character ensured by antibacterial NO and  $O_2(^1\Delta_g)$  species generated on the surface with increased wettability **iii)** the antibacterial action caused by photoreleased NO **iv)** the vasodilation effect caused by NO.

Binding of NO onto the dimetallaborane [*closo*-(PMe<sub>2</sub>Ph)<sub>4</sub>Pt<sub>2</sub>B<sub>10</sub>H<sub>10</sub>] was confirmed by visible colour-change and multi-nuclear NMR spectroscopy. It was also ascertained that NO release will probably require the use of UV light irradiation (as is the case for CO or SO<sub>2</sub>), which is a part of our continuing study. Seven new monometallic precursors were synthesized and characterized. The syntheses of new bimetallaboranes using these new compounds as precursors were not successful conceivably due to the extra steric bulk of the metal ligands. Nevertheless, the newly obtained monometallaboranes may well offer interesting properties and uses *e. g.* for further chemical modification or catalysis.

The incorporation of bimetallic cluster system in the nanofiber materials was beyond the scope of this thesis but it remains a part of the continuing research.

## 7. References

---

1. DeRosa, M.C., *et al. Coord. Chem. Rev.* **233**, 351 (2002).
2. Mikkelsen K. V., *et al. Photochemistry and photobiology* **70**:4, 369 (1999).
3. Lang, K., *et al. Coord.Chem.Rev.* **248**, 321 (2004).
4. Ross, A. B., *et al. J. Phys. Chem. Ref. Data*, **24**, 663 (1995).
5. Foote, C. S.; Clennan, E. L.: *Active Oxygen in Chemistry*, Vol. 2, Blackie Academic & Professional, London (1995).
6. Slanger, T. G., *et al. Chemical reviews*, **103**:12, 4731 (2003).
7. Schmidt, R., *et al. Acc. Chem. Res.* **36**, 668 (2003).
8. Lang, K., *et al. Chemické Listy* **99**, 211 (2005).
9. Hueder P. M. de Oliveira: *Phenotiazinium Dyes as Photosensitizers (PS) in Photodynamic Therapy (PDT): Spectroscopic Properties and Photochemical Mechanisms*, InTech (2012).
10. Tedesco, A. C., *et al. Biochim. Biophys. Acta-Biomembranes*, **223**, 1280 (1996).
11. Bonnett, R. *Chem. Soc. Rev.* **24**, 19 (1995).
12. Hynninen P. H., *et al. J. Photochem. Photobiol. B* **73**, 1 (2004).
13. Dougherty, T. J., *et al. J. Porphyrins Phthalocyanines*, **5**, 105 (2001).
14. Levy, J. G., *et al. Photochem. Photobiol.* **54**, 670 (1993).
15. Hasan, T., *et al. Photochem. Photobiol. Sci.* **3**, 436 (2004).
16. Wainwright, M. *Chem. Soc. Rev.* **31**, 128 (2002).
17. Jori, G. *et al. Insect Biochem. Mol. Biol.* **30**, 915 (2000).
18. Gamlin, J. N. *et al. Photochem. Photobiol.* **70**, 391 (1999).
19. Ross, A. B. *et al. J. Phys. Chem. Ref. Data* **22**, 113 (1993).
20. Wagnerová, D. M., *et al. Coord. Chem. Rev.* **248**, 321 (2004).
21. Ricchelli, F. *J. Photochem. Photobiol. B.: Biol.* **29**, 109 (2004).
22. Wagnerová, D. M., *et al. J. Photochem. Photobiol. A* **130**, 13 (2000).
23. Dolphin, D., *et al. Photochem. Photobiol.* **64**, 469 (1996).
24. Armitage, B. *Chem. Rev.* **98**, 1171 (1998).
25. Pandey, R. K., *et al. Bioconjugate Chem.* **10**, 94 (1999).
26. Jenkins, T. C., *et al. J. Am. Chem. Soc.* **121**, 1768 (1999).
27. Hurley, L. H., *et al. J. Am. Chem. Soc.* **121**, 3561 (1999).
28. Ashkenazi, H., *et al. Photochem. Photobiol.* **69**, 505 (1999).
29. Henke, P., *et al. ACS Appl. Mater. Interfaces*, **5**, 3776 (2013).
30. Neurath, R. A., *et al. J. Med. Chem.* **37**, 1099 (1994).
31. Plíštil, L., *et al. Photochem. Photobiol.* (2014) (submitted).
32. Ogilby, P. R., *et al. J. Am.Chem.Soc.* **118**:2, 388 (1996).
33. Mosinger, J., *et al. Experientia* **51**, 106 (1995).
34. Mosinger, J., *et al. J. Photochem. Photobiol. A* **107**, 77 (1997).
35. Senecal, K., *et.al. Adv. Mater.*, **34**, 44 (2002).
36. Mansfield, K., *et. al. J. Controlled Release*, **81**, 57 (2002).

- 
37. Huang, Z. M., *et. al. J. Mater. Sci.: Mater. Med.*, **16**, 933 (2005).
  38. Ku, B. C., *et.al. Nano Lett.*, **4**, 331 (2004).
  39. Mosinger, J., *et. al. J. Mater. Chem.*, **17**, 164 (2007).
  40. Mosinger, B., *et. al. J. Fluores.* **19**, 705 (2009).
  41. Jesenská, S., *et. al. J. Biomed. Mater. Res. A*, **99**, 676 (2011).
  42. Arenbergerová, M., *et.al. Exp. Dermatol.*, **21**, 619 (2012).
  43. Lhotáková, Y., *et. al. PLoS ONE*, **7**, e49226 (2012).
  44. Wendorff, J. H., *et.al. Angewandte Chem Int Ed*, **46**, 5670 (2007).
  45. Lin, C. P., *et.al. Biophys. J.*, **84**, 4023 (2003).
  46. Davies, M. J., *et. al. Free Radical Biol. Med.*, **47**, 92 (2009).
  47. Reinecke, H., *et. al. Macromolecules*, **45**, 2648 (2012).
  48. Sortino, S. *Chem. Soc. Rev.*, **39**, 2903 (2010).
  49. Casas, A., *et. al.: J. Photochem. Photobiol. B* **80**, 195 (2005).
  50. Chaplin, D. J. *et. al., Br. J. Cancer* **82**, 1835 (2002).
  51. Bishop, Ch. M.: *Development of a Nitric Oxide Measurement Method in Tissue Media*. Fort Collins, Colorado, Master Thesis. Colorado State University (2012).
  52. Janczuk, A. J., *et. al. Chemical Reviews*, **102** (4), 1091 (2002).
  53. Fang, F. C., *et. al. Journal of Clinical Investigation* **99** (12), 2818 (1997).
  54. Masharak, P. K., *et. al. Coord. Chem. Rev.* **252**, 2093 (2008).
  55. Condorelli, G., *et. al. Chem. Commun.*, **1226** (2001).
  56. Sortino, S., *et. al. Photochem. Photobiol. Sci.*, **7**, 911 (2008).
  57. Valli, L., *et. al. J. Mater. Chem.*, **18**, 2437 (2008).
  58. Deniz, E., *et. al. Chem. Eur. J.* **18**, 15782 (2012).
  59. Kandoth, N., *et. al. J. Mater. Chem. B*, **1**, 3458 (2013).
  60. Anindya, G., *et. al. 64th Southwest Regional Meeting of the American Chemical Society*, Abstract, (2008).
  61. Hasan, T.; Moor, A. C. E. and Ortel, B. *Cancer Medicine*, Decker BC Inc. Hamilton, Ontario, Canada, 5th ed, (2000).
  62. Nablo, N., *et. al. Biomaterials*, **26**, 917 (2005).
  63. Bohlender, C., *et. al. J. Mater. Chem.*, **22**, 8785 (2012).
  64. Vogt, C., *et. al. Biomacromolecules*, **14**, 2521 (2013).
  65. Bould, J., *et al., Inorg. Chem.* **50**, 7511 (2011).
  66. Greenwood, N. N. ; Earnshaw, A. *Chemistry of the Elements*. Headington Hill Hall, Oxford, England : Pergamon Press Plc (1984).
  67. Housecroft, C. E. . *Boranes and metallaboranes : structure, bonding and reactivity*. 2nd edition. Hertfordshire : Ellis Horwood Limited (1994).
  68. Kawasaki, Y. *et al., Nucl. Instrum. Meth. B*, **25**, 237 (2005).
  69. Kennedy, J. D.: *The Polyhedral Metallaboranes Part II. Metallaborane Clusters with Eight Vertices and More*, John Wiley & Sons, Inc., Hoboken, USA (1986).
  70. Staves, J., *et. al., J. Chem. Soc., Dalton Trans.*, 2573 (1981).
  71. Hawthorne, M. F., *et. al., J. Am. Chem. Soc.*, **100**, 3758 (1978).

- 
72. Thornton-Pett, M. *et al.*, *Inorg. Chem. Acta*, **99**, L43 (1985).
  73. Kennedy, J. D., *et al.*, *Chem. Commun.*, 2380 (2004).
  74. Cowie, M., *et al.*, *J. Am. Chem. Soc.*, **115**, 3212 (1993).
  75. Taube, H., *Prog. Inorg. Chem.*, **34**, 607 (1986).
  76. Minghetti, G., *et al.*, *Inorg. Chem.*, **22**, 2332 (1983).
  77. van Koten, G., *et al.*, *Chem.-Eur. J.* **6**, 1431 (2000).
  78. Pluth, S. J. *et al.*, *Chem. Commun.*, **48**, 11981 (2012).
  79. Bryan, N. Si., *et al. Free Radic Biol Med.*, **43**(5), 645 (2007).
  80. Kupková, Z., *et al. Chem. Listy*, **98**, 116 (2004).
  81. Huangxian, J. and Xueji, Z. *Electrochemical sensors, biosensors and their biomedical applications*. 1st ed. Amsterdam: Elsevier/Academic Press, (2008).
  82. Caruso, E. B., *et al. Chem. Commun.*, 5028 (2007).
  83. Sortino, S. *et al. J. Mater. Chem.*, **19**, 8253 (2009).
  84. Cicillini, S. A., *et al. Polyhedron*, **28**, 2766 (2009).
  85. Carneiro, Z. A., *et al. Journal of Inorganic Biochemistry*, **105**, 1035 (2011).
  86. Ratanatawanate, C., *et al. J. Am. Chem. Soc.* **133**, 3492 (2011).
  87. Sortino, S., *et al. Chem. Commun.*, 1971 (2008).
  88. Mortreux, A. *et al. Organometallics*, **14**, 401 (1995).
  89. Furukawa, N. *et al. Bul. Chem. Soc. Jpn.*, **64**, 3182 (2001).
  90. Navarro-Ranninger, C. *et al. Eur. J. Inorg. Chem.* 1591 (2003).
  91. Giotto, M. T. S. *et al. Transition. Met. Chem*, **20**, 380 (1995).
  92. Suman, P. *et al. Organometallics*, **17**, 4344 (1998).
  93. Paavola, S. *et al. J. Organomet. Chem.* **606**, 183(2000).
  94. Heřmánek, S. *Chem. Rev.*, **92** (2), 325 (1992).
  95. Crutchley, R. J. *et al. Coord. Chem. Rev.* **233/234**, 355 (2002).
  96. Villanueva, A. L. *et al. J. Photochem. Photobiol. B, Biol.* **23**, 49 (1994).
  97. Černý, J. *et al. Journal of Photochemistry and Photobiology A* **210**, 82 (2010).
  98. Henke, P. *et al. ACS Surfaces and Interfaces* (2014) (submitted).
  99. Atorngitjawat, P. *et al. Macromolecules* **40**, 991 (2007).
  100. Camacho, L. *et al. Langmuir*, **23**, 3794 (2007).
  101. Jianzhuang, J. *et al. Vibrational Spectroscopy* **32**, 175 (2003).
  102. Roberts, G. L. *et al. J. Mater. Chem.*, **13**, 1603 (2003).
  103. Skibsted, L. H. *et al. Chem. Rev.*, **102**, 1167 (2002).
  104. Kassner, R. J. *et al. Biochemistry*, **18**, 5387 (1979).
  105. Tzirakis, M. D. *et al., M. Org. Lett.*, **10**, 873 (2008).